Journal Pre-proof

Structural insights on the interaction potential of natural leads against major protein targets of SARS-CoV-2: Molecular modelling, docking and dynamic simulation studies

Sinosh Skariyachan, Dharshini Gopal, Aditi G. Muddebihalkar, Akshay Uttarkar, Vidya Niranjan

Please cite this article as: S. Skariyachan, D. Gopal, A.G Muddebihalkar, A. Uttarkar, V. Niranjan, Structural insights on the interaction potential of natural leads against major protein targets of SARS-CoV-2: Molecular modelling, docking and dynamic simulation studies, *Computers in Biology and Medicine*, https://doi.org/10.1016/j.compbiomed.2021.104325.

This is a PDF file of an article that has undergone enhancements after acceptance, such as the addition of a cover page and metadata, and formatting for readability, but it is not yet the definitive version of record. This version will undergo additional copyediting, typesetting and review before it is published in its final form, but we are providing this version to give early visibility of the article. Please note that, during the production process, errors may be discovered which could affect the content, and all legal disclaimers that apply to the journal pertain.

1 **Structural insights on the interaction potential of natural leads against major protein**

2 **targets of SARS-CoV-2: Molecular modelling, docking and dynamic simulation studies**

3

4 [1]Sinosh Skariyachan*, [2]Dharshini Gopal[#], [3]Aditi G Muddebihalkar, [3]Akshay Uttarkar, [3]Vidya

5 Niranjan

6

7 [1]Department of Microbiology, St. Pius X College Rajapuram, Kasaragod, Kerala, India

8 [2]Department of Bioinformatics, Manipal Academy of Higher Education, Manipal, Karnataka,

9 India

10 [3]Department of Biotechnology, RV College of Engineering, Bengaluru, Karnataka, India

11 [#]Joined first author, equally contributed

12 *Corresponding author: sinoshmicro@stpius.ac.in, sinoshskariya@gmail.com

13

14 **Abstract**

15 Though significant efforts are in progress for developing drugs and vaccines against COVID-

16 19, limited therapeutic agents are available currently. Thus, it is essential to undertake

17 COVID-19 research and to identify therapeutic interventions in which computational

18 modeling and virtual screening of lead molecules provide significant insights. The present

19 study aimed to predict the interaction potential of natural lead molecules against prospective

20 protein targets of SARS-CoV-2 by molecular modeling, docking, and dynamic simulation.

21 Based on the literature survey and database search, fourteen molecular targets were selected

22 and the three targets which lack the native structures were computationally modeled. The

23 drug-likeliness and pharmacokinetic features of ninety-two natural molecules were predicted.

24 Four lead molecules with ideal drug-likeliness and pharmacokinetic properties were selected

25 and docked against fourteen targets, and their binding energies were compared with the

26 binding energy of the interaction between Chloroquine and Hydroxychloroquine to their

27 usual targets. The stabilities of selected docked complexes were confirmed by MD simulation

28 and energy calculations. Four natural molecules demonstrated profound binding to most of

29 the prioritized targets, especially, Hyoscyamine and Tamaridone to spike glycoprotein and

30 Rotiorinol-C and Scutifoliamide-A to replicase polyprotein-1ab main protease of SARS-

31 CoV-2 showed better binding energy, conformational and dynamic stabilities compared to the

32 binding energy of Chloroquine and its usual target glutathione-S-transferase. The

33 aforementioned lead molecules can be used to develop novel therapeutic agents towards the

34 protein targets of SARS-CoV-2, and the study provides significant insight for structure-based

35 drug development against COVID-19.

36

39

1. Introduction

40

41 Severe Acute Respiratory Syndrome Coronavirus (SARS-CoV-2) is responsible for

42 Coronavirus disease-2019 (COVID-19), formerly known as nCoV-2019, which was first

43 reported in the city of Wuhan, China in December 2019 [1]. Globally, 116 million confirmed

44 cases and 2.58 million deaths have been reported as of the first week of March 2021 as per

45 the latest reports of the World Health Organization (WHO) [2]. The WHO declared COVID-

46 19 as a pandemic due to the impact of a global outbreak, and the severity of the infection

47 caused by SARS-CoV-2 [3]. It is one of the challenging outbreaks the world has ever

48 experienced, and most of the developed countries are at the risk of community outbreaks [4,

49 5, 6]. While there were several asymptomatic cases reported, the infection mainly

50 characterized by the symptoms such as fever, muscle and body aches, cough, sore throat,

51 shortness of breath for about 5-6 days after the infection, whereas, it causes a severe form of

52 pneumonia in the elderly and immune-compromised people that resulted in worldwide panic

53 leading to an international concern [7, 8, 9, 10]. Presently, more than 90% of the deaths are

54 reported due to COVID-19, and the major countries with high mortality rates reported include

55 the United States of America, India, Brazil, Russian Federation, The United Kingdom,

56 France, Spain, Italy, Turkey, Germany, Colombia and Argentina [2]. Currently, there are

57 limited therapeutic agents available for the treatment of COVID-19, which demonstrates the

58 severity of the infection. Thus, it is essential to undertake COVID-19 research and to screen

59 putative drug targets and lead molecules for the development of therapeutic strategies

60 towards COVID-19.

61

62 The surface spike proteins (S), membrane proteins (M), envelope proteins (E), main protease-

63 replicase polyproteins (rep and protein 1a), and few non-structural proteins (nsp6, nsp8, and

64 nsp10) are responsible for the pathogenesis mechanism of coronavirus [10]. Spike

65 glycoproteins protruding on the surface of the virus mediates the viral entry into the host cells

66 [11, 12]. Five regions were identified in spike proteins (residues 274–306, 510–586, 587–

67 628, 784–803, and 870–893) that represent the regions associated with the high rate of an

68 immune response [13]. The nucleoprotein such as replicase polyprotein and RNA-dependent

69 RNA polymerase (RdRp) played a pivotal role in the virus replication and form a

70 ribonucleoprotein complex with the viral RNA through the N-terminal domain (N-NTD) of

71 protein N. The membrane protein involved in the protein-protein interactions required for

72 assembly of coronaviruses, and determined as a protective antigen in humoral responses

3

73   which functions as an ion channel [14]. Replicase polyproteins such as main protease (Mpro)

74   and papain-like protease (PLpro) are involved in the cleavage of polyproteins, and non-

75   structural proteins (nsp) are involved in the assembly of replicase-transcriptase complex

76   (RTC) [14, 15, 16]. Therefore, these proteins can be considered as potential targets to develop

77   therapeutic agents against SARS-CoV-2.

78

79   The drugs that were suggested in the treatment of COVID-19 include Hydroxychloroquine,

80   Chloroquine, Ritonavir, Lopinavir, and Remdesvir, which are used for the treatment of

81   Malaria, AIDS, Ebola, and Influenza [17, 18]. Hence, there is a need to screen more reliable

82   approaches to combat the infections caused by SARS-CoV-2. Computational biology studies

83   are one of the promising approaches to reduce the time and cost of various stages of drug

84   discovery when compared to the conventional methods of drug development. The major

85   approaches of computational biology in drug discovery include molecular modeling of

86   potential targets, computer-aided virtual screening of novel lead molecules, and molecular

87   dynamic simulation studies of the target-lead complexes. These methods can be used to

88   screen potential lead molecules against SARS-CoV-2. Several studies have demonstrated that

89   the bioactive molecules from natural sources can be used to treat several viral infections

90   because the natural compounds possess fewer side effects, ideal drug likeliness,

91   pharmacokinetic and toxicity properties, and their binding potential to the molecular targets

92   [19, 20].

93

94   The present study aimed to predict the binding potential of selected natural leads against

95   multiple protein targets of SARS-CoV-2 when compared to the binding of two currently

96   suggested drugs to their usual targets by computational virtual screening, molecular

97   modeling, and dynamic simulation studies.

98

99   **2. Materials and methods**

100   2.1. Identification of probable molecular targets

101   The drug targets of SARS CoV – 2 were identified based on the literature survey, database

102   search, and knowledge on their role in pathogenicity especially mediating host cell and

103   replication of RNA. The major targets involved in the virulence mechanism of SARS-CoV-2

104   are spike glycoproteins, replicase, membrane proteins, envelope proteins, and non-structural

105   proteins. A total of fourteen probable drug targets, namely protein S, E, M5, rep, 1a, 7a, 3a,

106   nsp6, nsp7, nsp8, 9b, nsp10, nsp12, and receptor-binding domain (RBD) were identified as

107   potential molecular targets. Out of fourteen targets identified, the three-dimensional (3D)

108   structures of S, E, M5, rep, 1a, Protein7a, Protein9b, nsp7, nsp8, nsp12, and RBD are

109   available in their native forms. The structural details of the selected targets are shown in

110   **Table 1**. The 3D structures of spike glycoprotein available in post-fusion (PDB: 1WYY;

111   resolution: 2.2Å) [22], open state (PDB: 6VYB; resolution 3.2Å) [10] and closed state (PDB:

112   6VXX; resolution 2.8Å) [10] were retrieved from protein data bank (PDB) [21]. Similarly,

113   the structures of the main protease (Mpro) (PDB: 1Q2W; resolution 1.8Å) [23], Mpro (PDB:

114   5RE4; resolution 1.88Å) [24], membrane protein (chain C, F) (PDB: 3I6G; resolution

115   2.201Å) [25], envelope protein (PDB: 2MM4) [26], Protein7a (PDB: 1XAK; resolution

116   1.8Å) [27], Protein9b (PDB: 2CME; resolution 2.8Å) [28], ribosome binding protein (RBD)

117   (PDB: 6M17; resolution 2.9Å) [29], RNA dependent RNA polymerase (RdRp) (PDB: 6M71;

118   resolution 2.9Å) [30] with chain A (non-structural protein 12; nsp12), chain B and D (non-

119   structural protein 7; nsp7), and C (non-structural protein 8; nsp8) were selected as a drug

120   target.

121

122   2.2. Model building and validation

123   Out of fourteen identified targets, the 3D structures of three proteins namely Protein3a, nsp6,

124   and nsp10 were not reported in their native forms. Thus, the amino acid sequences of

125   Protein3a (UniProt ID: P59632), nsp6 (UniProt ID: P59634), and nsp10 (UniProt ID:

126   P0C6U8) were retrieved from UniProt KB [31], and the 3D structures of these proteins were

127   predicted from the basic amino acid sequences by *ab initio* (*de novo*) modelling by C-I-

128   Tasser [32]. The 3D models of three targets were energy minimized by ModRefiner [33]. The

129   secondary structures of the hypothetical models were assessed by STRIDE [34]. The

130   hypothetical models were analyzed and computationally validated by ProSa [35], Verify3D

131   [36], ProCheck [37], ERRAT [38], and ANOLEA [39] in terms of the reliability, model

132   quality, stereochemical quality (Ramachandran plot), quality factor (error function), structural

133   and force field parameters, respectively.

134

135   2.3. Identification and virtual screening of natural lead molecules

136   Based on the relevance of natural compounds in medicinal chemistry research, the lead

137   molecules present in various natural sources like plants and microorganisms with antiviral

138   properties were identified by literature survey and database search. The details of these

139   compounds are shown in Supplementary Material, Table S1. A total of ninety-two natural

140   compounds were identified, and their 3D structures were retrieved from PubChem [40] and

141   Chemspider [41] databases in .sdf and. mol formats, respectively (Supplementary Materials,

142   Table S1). The retrieved sdf files were converted into .pdb by Open Babel [42]. The drug

143   likeliness, pharmacokinetics (adsorption, distribution, metabolism, excretion -ADME), and

144   toxicity properties were predicted using the molecular descriptors, filters, and statistical

145   models available at PreADMET [43] and SwissADME [44]. The molecular filters used to

146   predict drug likeliness included Lipinski's rule of five [45], Comprehensive Medicinal

147   Chemistry (CMC) rule, Egan's rule [46], MDL Drug Data Report (MDDR) like rule [47],

148   World Drug Index (WDI) like rule, Ghose filter [48], lead-like rule [49] and bioavailability

149   score [50]. The statistical models such as blood-brain barrier (BBB) [51], caco2 cell

150   permeability [52], human intestinal absorption (HIA) [53], lipophilicity [54], and water

151   solubility [55] were predicted by PreADMET and SwissADME. The statistical models such

152   as daphnia toxicity, Ames test [56], algae test, hERG inhibition, carcinogenicity in rats and

153   mice, Minnow and Medaka fish toxicity and mutagenicity in terms of TA100_NA (-S9),

154   TA1535_10RLI (-S9), TA100_10RLI (þS9), and TA1535_NA (þS9) strain of *Salmonella*

155   *typhimurium* were used to predict the toxicity features. The molecules that qualified the

156   features required for drug likeliness, pharmacokinetics, and toxicity were selected.

157

158   2.4. Molecular docking studies

159   Four potential molecules that qualified the drug-likeliness, ADME, and toxicity properties

160   were selected, and the binding potentials of these molecules to fourteen selected targets of

161   SARS CoV-2 were predicted using molecular docking by AutoDock tools and AutoDock

162   Vina [57]. The binding sites of selected target proteins were predicted by Depth [58] and

163   CastP [59]. The protein targets were prepared by adding polar hydrogen atoms and Gasteiger

164   partial charges. The ligands were prepared by setting the number of torsions and detecting the

165   root atoms. The ligand and receptor files were written in. PDBQT format. The grid box for

166   each target was prepared based on the dimensions of x, y, z coordinates of the binding

167   pocket, and the configuration file was prepared. Each ligand molecule was docked against the

168   selected target, and the output log files were prepared. Out of various docked conformations,

169   the best-docked poses of the complexes were selected based on the binding energy

170   (kcal/mol), cluster RMSD, number of hydrogen bonds, and other weak interactions, which

171   stabilised the docked complexes. The binding energies associated with the interaction

6

172 between natural molecules and selected targets were compared with the binding energy of the

173 interaction between Chloroquine and Hydroxychloroquine towards their usual targets namely

174 glutathione S transferase (PDB: 1OKT) of *Plasmodium falciparum* and human angiotensin-

175 converting enzyme (ACE)-2 (PDB: 1R42), respectively. The results of these docked

176 complexes were considered as the control for the comparison of the binding potential of

177 natural molecules and the selected targets.

178

179 2.5. Molecular dynamic simulation studies

180 The molecular dynamic (MD) simulation studies were performed to confirm the stabilities of

181 the best-docked complexes of ligands and their targets along with the interaction of

182 Chloroquine and glutathione S transferase. The MD simulation was performed by the

183 Desmond module of Schrödinger's suite [60]. The protein-ligand complexes were subjected

184 to pre-processing and hydrogen bond assignment was performed with standard parameters.

185 The simulation system was prepared by utilizing the system builder. TIP3P was selected as

186 the solvent model, and the boundary conditions were defined by an orthorhombic box with

187 minimized volume encapsulating the complex. OPLS3e was used as a force field, and the

188 system neutralized by adding Cl^- or Na^+ ions based on the total charges of the system. The

189 MD simulations were performed at 300 K using the constant number of particles, pressure,

190 and temperature (NPT) ensembles for 100 ns at an interval of 1ns. The model was unfitted for

191 10ns before performing the MD simulation. The time-step adjusted to 2 femtoseconds (fs), a

192 short-range cut-off with a radius of 9.0 Å optimized, and no restraints were pre-defined. The

193 simulation showed a temperature increase of 10K per time-step after the solvation of the

194 binding pocket. The changes in RMS and protein-ligand contacts during simulation were

195 generated by the simulation interaction diagram tool

196 The trajectories of RMSD and RMSF of proteins and ligands were estimated using the

197 following formula:

198

$$RMSD_X = \sqrt{\frac{1}{N}\sum_{i=1}^{N}\left(r_i^t(t_x) - r_i(t_{ref})\right)^2}$$

199

200

7

201　Where N is the number of atoms in the atom selection; t_{ref} is the reference time, (first frame

202　used as reference, time t = 0); and r' is the position of the selected atoms in frame x after

203　superimposing on the reference frame, where frame x is recorded at time t_x.

$$RMSF_i = \sqrt{\frac{1}{T}\sum_{t=1}^{T} < \left(r'(t) - r_i(t_{ref})\right)^2 >}$$

204

205　Where, T is the trajectory time over which the RMSF calculated, t_{ref} is the reference time

206　(time t = 0); r is the position of an atom in the reference at time t_{ref}, and r' is the position of

207　atom at time t after superimposing on the reference frame.

208

209　The protein-ligand RMSD, protein and ligand RMSF, protein-ligand contacts, ligand

210　properties, and ligand torsion profile trajectories were analyzed using the simulation

211　interaction diagram tool.

212

213　2.6. Molecular mechanics Poisson-Boltzmann surface area (MM-PBSA) calculations

214　The calculation of model affinities of each docked complex (protein-ligand interactions) after

215　a minimal simulation period of 1ns performed by GROMACS [61, 62, 63] using

216　CHARMM36 all-atom force field. CGenFF (Force field generator) was used to assign the

217　parameters and charges to ligand to generate an index file. A solvation dodecahedron box

218　generated with TIP3P solvent, and ions were added to neutralize the system charges. The

219　energy minimization was carried out at 0.5 ns. Equilibration of the number of particles,

220　volume, and temperature (NVT) ensemble was carried out before producing molecular

221　dynamics of 1ns. The trajectory files generated were used as the input files. The calculation

222　of energy by MMPBSA carried out using the following command:

223　g_mmpbsa -f traj.xtc -s topol.tpr -n index.ndx -mme -mm energy_MM.xvg

224　The output was reported in terms of binding energy (kcal/mol).

225

226　**3. Results and discussion**

227　3.1. Prospective molecular targets

228　Fourteen target proteins namely protein S, M, E, rep, 1a, 3a, 7a, 9b, nsp6, nsp7, nsp8, nsp10,

229　nsp12, and RBD were identified based on an extensive literature survey and database search.

230　Eleven targets possessed native structures (**Table1**), and three targets, which lack the 3D

231　structures were computationally modeled (**Table 2**). Spike glycoprotein S (PDB: 1WYY,

232   6VXX, 6VYB) was identified to be one of the most important targets due to its involvement

233   in mediating host transfer by attaching the virion to the cell surface, and interacting with the

234   host, and promote the infection [64, 65]. The post-fusion conformation of the spike

235   glycoprotein is a hairpin structure comprised of two heptad repeats that are stabilized by

236   Asparagine and Glutamine residues, and form hydrogen bonds between the two heptad

237   domains. The open and closed conformations of the surface spike glycoprotein act as an

238   important part of interaction with the host cell surface and, three human Angiotensin-

239   Converting Enzyme 2 (hACE2) motifs were observed in the closed conformation, thus, the

240   conformation is important for the interaction with hACE2 at host cell surface initiating the

241   viral entry [10]. The receptor-binding domain of the membrane protein interacted with the

242   human cellular receptor hACE2 that recognizes SARS CoV-2 [29]. The membrane protein M

243   is involved in morphogenesis, envelope membrane protein E induces apoptosis by activating

244   host inflammasome, and replicase protein rep involved in transcription and replication of

245   viral RNA, which contain proteinases that cleave the polyprotein [66, 67]. Replicase

246   polyprotein 1a is a proteinase that cleaves the N and C- terminal of replicase polyprotein and

247   involved in suppressing the host gene expression [68]. RNA-dependent RNA polymerase

248   consists of three non-structural proteins namely nsp7, nsp8, and nsp12 [30]. Protein3a

249   induces apoptosis [69], protein 7a involved in the viral replication in cell culture [70],

250   Protein9b is a lipid-binding protein, non-structural protein6 (nsp6) initiates induction of

251   autophagosomes, non-structural protein8 (nsp8) acts as primase in the viral replication and

252   non-structural protein10 (nsp10) involved in viral mRNA cap methylation [71, 72, 73].

253   Therefore, based on the functional role and virulence mechanisms, these proteins were

254   considered to be putative molecular targets for drug screening in the present study.

9

255   **Table 1.** The structural description of eleven probable drug targets (with known 3D structures) that are involved in the virulence and pathogenesis of SARS-CoV-2
256

PDB ID	Name of the protein	Chain	Resolution	R-Value Free	R-Value Work	Experimental method	Secondary structure	References
1WYY	Post-fusion hairpin conformation of the spike glycoprotein	A, B	2.2 Å	0.249	0.210	X-ray diffraction	66% helical	Duquerroy et al., 2005
6VYB	SARS-CoV-2 spike ectodomain structure (open state)	A, B, C	3.2 Å	Aggregation state: Particle	Reconstruction method: Single particle	Electron Microscopy	16% helical, 25% beta sheet	Walls et al., 2020
6VXX	Structure of the SARS-CoV-2 spike glycoprotein (closed state)	A, B, C	2.8Å	Aggregation state: Particle	Reconstruction method: Single particle	Electron Microscopy	16% helical, 25% beta sheet	Walls et al., 2020
1Q2W	X-Ray Crystal Structure of the SARS Coronavirus Main Protease	A, B	1.86 Å	0.249	0.194	X-ray diffraction	24% helical, 28% beta sheet	Bonanno et al., 2003
5RE4	Crystal Structure of SARS-CoV-2 main protease in complex with Z1129283193	A	1.88Å	0.266	0.199	X-ray diffraction	26% helical, 28% beta sheet	Fearon et al., to be published
3I6G	Newly identified epitope Mn2 from SARS-CoV M protein complexed withHLA-A*0201	C, F	2.201Å	0.246	0.205	X-ray diffraction	26% helical, 39% beta sheet	Liu et al., 2010
2MM4	Structure of a Conserved Golgi Complex-targeting Signal in Coronavirus Envelope Proteins	A	-	Conformers Calculated: 200	Conformers Submitted: 15	NMR	65% helical	Li et al., 2014
1XAK	Structure of the sars-coronavirus orf7a accessory protein	A	1.8Å	0.275	0.223	X-ray diffraction	48% beta sheet	Nelson et al., 2005
2CME	The crystal structure of SARS coronavirus ORF-9b protein	A	2.8Å	0.289	0.266	X-ray diffraction	3% helical, 44% beta sheet	Meier et al., 2006
6M17	The 2019-nCoV RBD/ACE2-B0AT1 complex	E, F	2.9Å	Aggregation state: Particle	Reconstruction method: Single particle	Electron Microscopy	3% helical, 23% beta sheet	Yan et al., 2020
6M71	SARS-Cov-2 RNA-dependent RNA polymerase in complex with cofactors	A, B. C, D	2.9Å	Aggregation state: Particle	Reconstruction method: Single particle	Electron Microscopy	47% helical, 17% beta sheet	Gao et al., 2020

257
258

259 **Table 2**. The description of computational validation of three probable drug targets of SARS-CoV-2 that are involved in the pathogenesis mechanism of coronavirus modeled
260 by *ab initio* approach using the C-I Tasser server.
261

UniProt ID	Organism	Entry names	Protein names	Gene	Function	Length	ProSA (z-score)	ERRAT (overall quality factor)	WHATIF Ramachandran (Z-score)	Verify3D (residues having averaged 3D-1D score >= 0.2)	Anolea (e/kt)	ProCheck		
												Favoured region	Allowed region	Outlier region
P59632	Human SARS coronavirus (SARS-CoV)	AP3A_CVHSA	Protein 3a	3a	induces apoptosis	274	-3.33	39.62	-5.763	50.82%	359	69%	35.8%	5.2%
P0C6U8	Human SARS coronavirus (SARS-CoV)	R1A_CVHSA	Non-structural protein 10	Nsp10	essential for viral mRNA cap methylation	139	-4.88	30.71	-6.042	63.64%	871	68.8%	27.9%	3.2%
P59634	Human SARS coronavirus (SARS-CoV)	NS6_CVHSA	Non-structural protein 6	Nsp6	induction of autophagosomes	63	-5.67	86.84	0.783	64.65%	-528	89.3%	9.1%	1.6%

11

262 3.2. Hypothetical model building and validation of selected targets

263 The 3D structures of target proteins such as Protein3a, non-structural protein6, and non-

264 structural protein10, which lack native structures were computationally predicted. The

265 sequence size of Protein3a, 6, and 10 were 274, 63, and 139 amino acids, respectively. The

266 3D structures of these sequences were predicted by C-I-Tasser, which utilizes deep-

267 convolutional neural-network-based contact-map prediction [32].

268

269 The theoretical model of Protein 3a is shown in **Fig. 1a**. The energy of the modeled protein

270 predicted by Anolea was found to be 1716e/kt, and energy was minimized to 879e/kt by

271 ModRefiner **(Table 2)**. The secondary structure of modeled protein comprised of 26.18,

272 29.82, 10.18, 33.82 alpha-helices, beta-sheet, beta turns, and coils, respectively **(Fig.1b)**.

273 Ramachandran plot of the model suggested that 69%, 35.8%, and 5.2% residues were located

274 in the most favored region, additionally allowed region, and outlier region of the plot,

275 respectively **(Fig. 1c)**. The stereo-chemical validation in terms of z-score obtained from

276 ProSA was found to be -4.88, which is comparable to the z-score of experimental structures

277 **(Fig. 1d)**. The VERIFY3D plot indicated that 63.64% of the residues possessed a 3D-1D

278 score of >=0.2, suggested a good quality model **(Fig.1e)**. The Z-score predicted by WHATIF

279 showed a value of -6.042 **(Table 2)**. The overall quality of the model is predicted to be 30.71

280 **(Fig. 1f)**. Thus, based on the computational validation, it is suggested that the hypothetical

281 model of Protein 3a showed good stereochemical validity, secondary structural alignment,

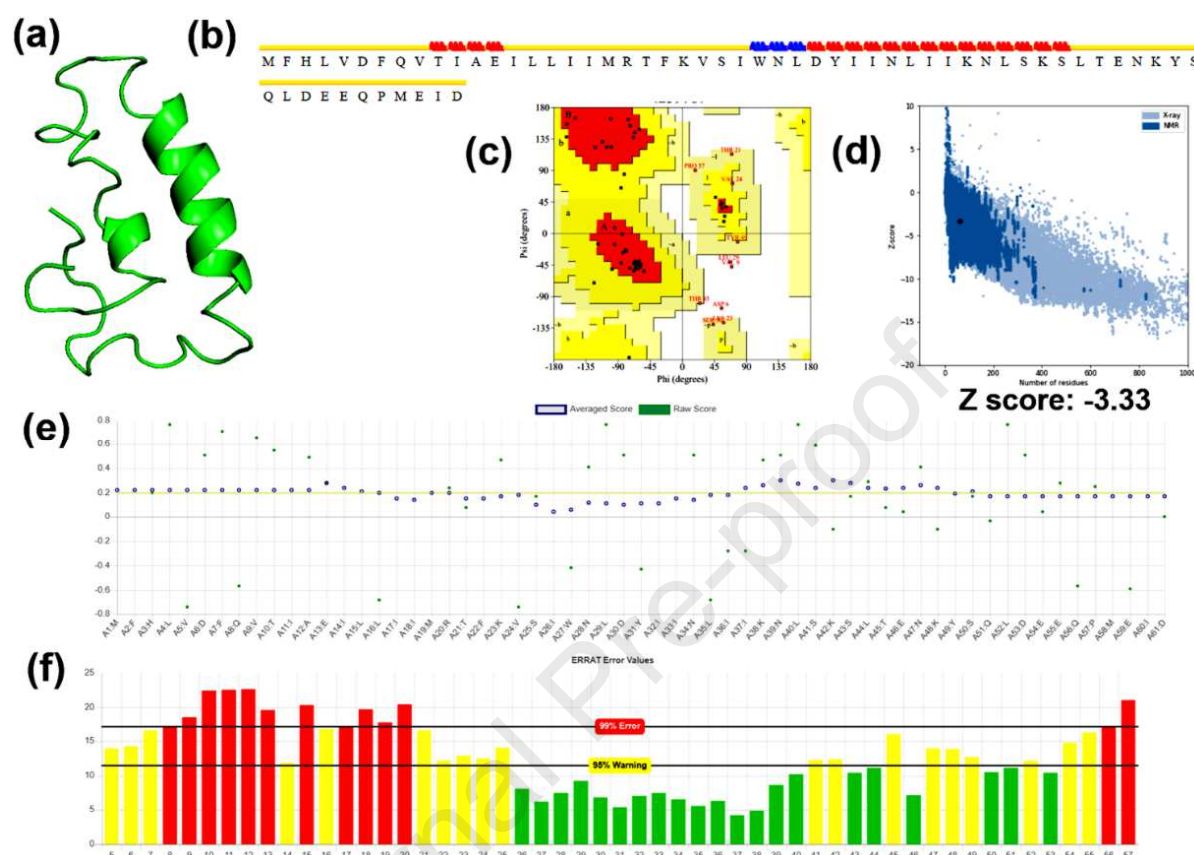282 and potential energy, which can be used as a molecular target.
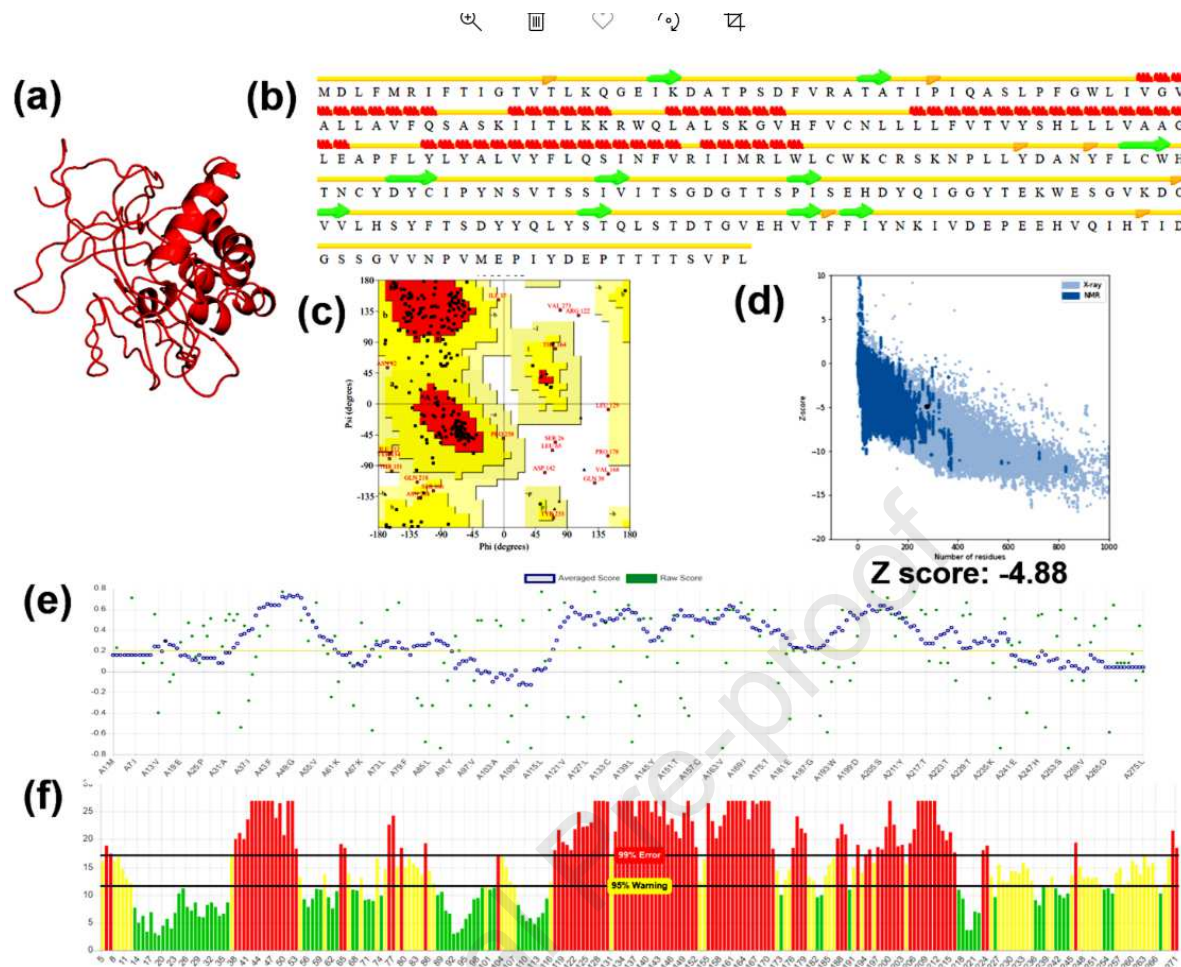
283

284

Fig.1. Computational modeling and model validation of Protein3a (a) Theoretical model of the target protein modeled using C-I-Tasser, (b) Secondary structure prediction of the theoretical model by STRIDE (c) Ramachandran plot assessment of the modeled residues of the target protein obtained by ProCheck (d) Stereo-chemical validation of the theoretical model in terms of z-score obtained from ProSA (e) The residues qualifying the 3D-1D score predicted by Verify 3D (f) The quality factor of the model obtained by the output plot of error function predicted by ERRAT.

The hypothetical model of nsp6 visualized by PyMol is illustrated in **Fig. 2a**. The energy of the protein model was minimized from 366e/kt to 359e/kt by ModRefiner. The secondary structure of the model comprised 70.4, 9.84, 8.20, and 11.48 % alpha-helices, beta-sheet, beta turns, and coils, respectively (**Fig. 2b)**. A Ramachandran plot of the model is shown in **Fig. 2c**, which revealed that 89.3%, 9.1%, 1.6% of the residues were present in the most favored region, additionally allowed regions, and outlier regions of the plot, respectively. The stereo-chemical validation by ProSA in terms of Z-score was found to be -3.33, a score closer to the z-score of native structures **(Fig. 2d)**. The plot obtained by VERIFY3D indicated that 50.82% of the residues showed a 3D-1D score of >=0.2 **(Fig. 2e)**. The Z-score predicted by WHATIF was found to be -5.67 **(Table 2)**. The overall model quality was found to be 39.62 **(Fig. 2f)**.

303 From the computational prediction, it was evident that the hypothetical model demonstrated

304 structural and stereochemical qualities, thus, the model can consider as a potential molecular
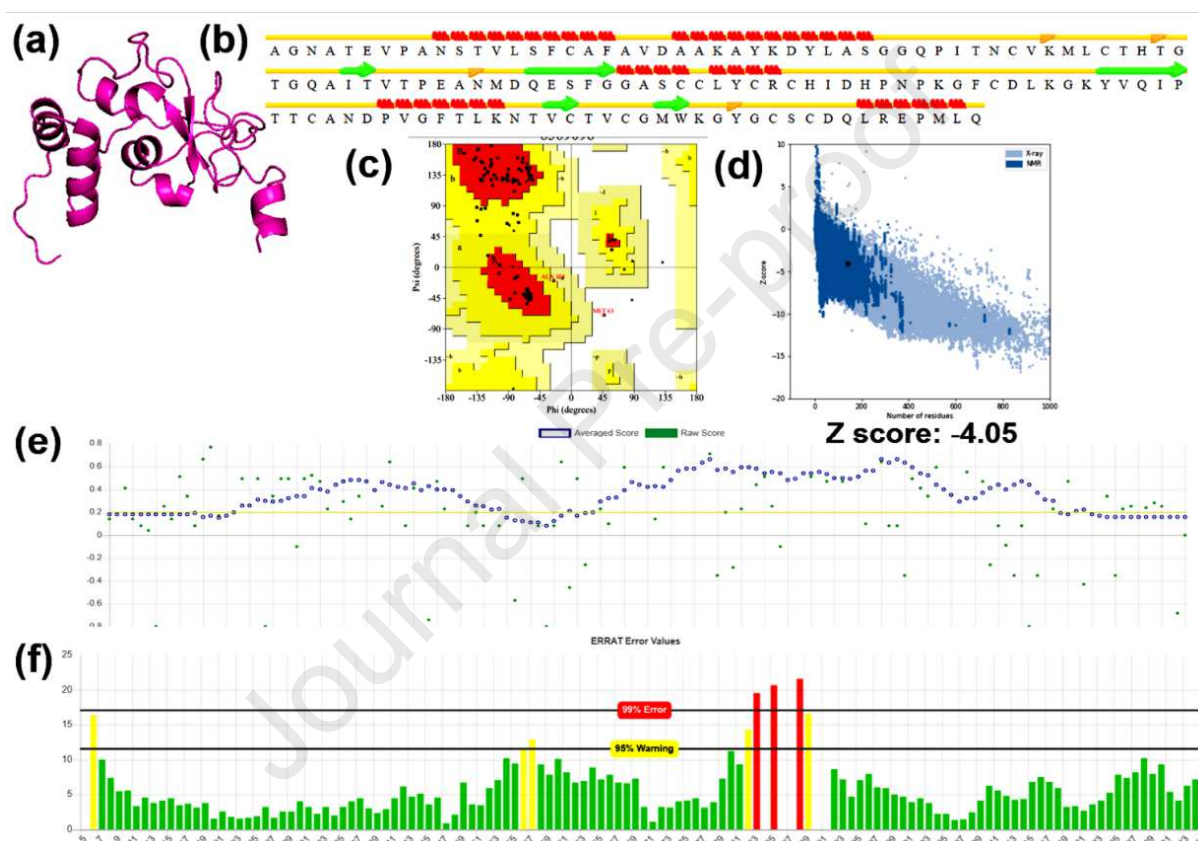
305 target.

306

307

308 **Fig.2**. Computational modeling and model validation of Protein6 (a) Theoretical model of the
309 target protein modeled using C-I-Tasser, (b) Secondary structure prediction of the theoretical
310 model by STRIDE (c) Ramachandran plot assessment of the modeled residues of the target
311 protein obtained by ProCheck (d) Stereo-chemical validation of the theoretical model in
312 terms of z-score obtained from ProSA (e) The residues qualifying the 3D-1D score predicted
313 by Verify 3D (f) The quality factor of the model obtained by the output plot of error function
314 predicted by ERRAT.

315

316 Similarly, the hypothetical model of nsp10 is shown in **Fig. 3a**. The energy of the protein

317 model was minimized from -636e/kt to -740e/kt **(Table 2)**. The secondary structure of the

318 modeled protein comprised 19.4, 25.9, 11.51, and 43.17 % of alpha-helices, beta-sheet, beta

319 turns, and coils, respectively **(Fig. 3b)**. Ramachandran plot of the model predicted by

320 ProCheck showed that 68.8, 27.9, and 3.2 residues were located in the favored, allowed, and

321 outlier regions, respectively **(Fig. 3c)**. The stereo-chemical quality obtained from ProSA was

322 found to be -4.05 in terms of Z-score, which was in the range of the z-score of the

14

323 experimental structures **(Fig. 3d)**. The plot of the theoretical model obtained by VERIFY3D

324 indicated that 70.5% of the residues were found to be a 3D-1D score of >=0.2 **(Fig. 3e)**. The

325 Z-score predicted by WHATIF showed a value of 0.334 (Table 2). The quality of the model

326 validated by ERRAT showed that a quality factor of 93.6 **(Fig. 3f)**. Therefore, the

327 computational validation showed that the 3D model of nsp10 was ideal in terms of

328 stereochemical and structural stabilities, and the model can be considered as a target for the

329 lead screening.

330

331

332 **Fig.3**. Computational modeling and model validation of Protein10 (a) Theoretical model of
333 the target protein modeled using C-I-Tasser, (b) Secondary structure prediction of the
334 theoretical model by STRIDE (c) Ramachandran plot assessment of the modeled residues of
335 the target protein obtained by ProCheck (d) Stereo-chemical validation of the theoretical
336 model in terms of z-score obtained from ProSA (e) The residues qualifying the 3D-1D score
337 predicted by Verify 3D (f) The quality factor of the model obtained by the output plot of error
338 function predicted by ERRAT

339

340 3.3. Computational screening of natural lead molecules
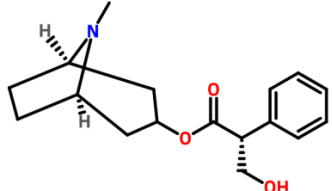
341 The virtual screening of 92 natural compounds from PubChem and ChemSpider databases

342 showed that 48 of them were qualified for the drug-likeliness predicted by various filters

343 available at PreADMET and SwissADME. The predicted drug-likeliness of natural lead

15

344 molecules is shown in Supplementary Material, Table S2. When 48 lead molecules were

345 subjected to ADME prediction, 16 compounds demonstrated ideal skin and caco2 cell

346 permeabilities, human intestinal absorption, blood-brain barrier penetration, gastrointestinal

347 absorption, lipophilicity, and water-solubility. The ADME features of the selected molecules

348 are shown in Supplementary Material, Table S3. When sixteen molecules that qualified the

349 ADME properties were screened for toxicity prediction, four molecules were qualified the

350 toxicity features such as carcinogenicity, mutagenicity, algae and fish toxicity, and hERG

351 inhibition. Thus, out of 92 molecules screened by *in silico* approach, four molecules were

352 qualified for drug-likeliness, ADME, and toxicity features. The selected molecules were

353 Hyoscyamine, Rotiorinol-C, Scutifoliamide-A, and Tamaridone, which are present in *Datura*

354 *stramonium*, *Chaetorium cupreum*, *Piper scutifolium*, and *Tamarix dioica*, respectively.

355 These natural compounds were prioritized as the lead molecules, and their interactions

356 towards fourteen molecular targets of SARS-CoV-2 were computationally modeled and

357 validated.

358

359 3.4. Molecular docking studies

360 The binding potential of selected natural lead molecules namely Hyoscyamine, Rotiorinol-C,

361 Scutifoliamide-A, and Tamaridone towards fourteen molecular targets (S, M, E, rep, 1a, 3a,

362 7a, 9b, nsp6, nsp7, nsp8, nsp10, nsp12, and RBD) of SARS-CoV-2 were predicted by

363 molecular docking. The best-docked conformations generated were analyzed and scrutinized

364 based on binding energy (kcal/mol), the number of hydrogen bonds and other stabilizing

365 interactions, and cluster RMSD. The binding potentials of four selected natural molecules to

366 the prioritized targets of SARS-CoV-2 were predicted by molecular docking studies are
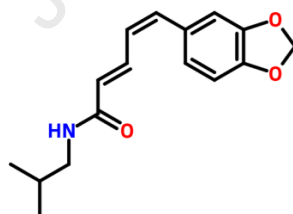
367 shown in **Table 3.**

16

368 **Table 3.** The binding potential of selected natural lead molecules towards the probable drug targets of human SARS-CoV-2 predicted by molecular docking studies
369

Protein name	PDB ID	Ligand names	Ligand structure	Binding affinity (Kcal/mol)	RMSD (Å)	Interacting residues	Hydrogen bonds
Spike glycoprotein	1WYY	Hyoscyamine Pubchem ID: 154417 Source: *Datura stramonium*		-8.14	0.0	Ser924, Thr925, Gly928, Asp932, Gln1161, ILe1164, Asn1168 (Chain A), Ser924, Thr925, Gly928, Gln1161, Ile1164 (Chain B)	Asn1168: 2
Spike glycoprotein-Closed state	6VXX			-5.7	0.0	Leu335, Pro337, Phe338, Gly339, Asp364, Val367	0
Spike glycoprotein-Open state	6VYB			-6.0	0.0	Trp104, Ile119, Val126, Ile128, Tyr170, Ser172, Ile203, Val227	Ser172: 1
Membrane protein	3I6G			-0.7	0.0	Gly0	0
Envelope small membrane protein	2MM4			-2.2	0.0	Lys63, Asn64	0
Replicase polyprotein 1ab	1Q2W			-6.1	0.0	Glu156, Met165, Asp187, Arg188, Gln189, Gln192	Gln192
Replicase polyprotein 1a	5RE4			-6.0	0.0	Trp218, Asn221, Leu271	Trp218: 1
Protein 7a	1XAK			-4.4	0.0	Tyr3, Tyr5, His47, Gln61	0
Protein 9b	2CME			-4.4	0.0	Arg68, Ala69, Phe70	0
Receptor binding domain of membrane protein	6M17			-5.4	0.0	Thr376, Val407, Ala411, Val433, Tyr508	0
Non-structural protein 7	6M71_C			-5.3	0.0	Thr46, Phe49, Val53	0

17

Protein	PDB ID	Compound	Binding energy		Interacting residues	H-bonds
Non-structural protein 8	6M71_B, D		-5.9	0.0	Leu128, Val130, Thr141, Tyr149	0
Non-structural protein 12	6M71_A		-5.4	0.0	Pro412, Phe415, Phe440, Phe843,	0
Non-structural Protein 6	Hypothetical model		-5.2	0.0	Asp6, Phe7, Leu15, Leu40, Ile60	0
Non-structural Protein 10	Hypothetical model		-6.1	0.0	Ile55, Cys74, Tyr76, His83, Asp91, Leu112, Thr115, Val116	His83:1
Protein 3a	Hypothetical model		-5.3	0.0	Phe56, Ile63, Lys66, Tyr189, Glu191,	0
Spike glycoprotein	1WYY	Rotiorinol C Pubchem ID: 11703984 Source: *Chaetorium cupreum*	-9.82	0.0	Arg4, Lys5, Tyr126, Gln127, Arg131, Asp289 and Glu290	5, Lys5, Gln127, Asp289, Glu290 (A chain) Glu127 (B chain)
Spike glycoprotein-Closed state	6VXX		-6.2	0.0	Arg34, Thr208, Pro209, Leu212, Pro217, Gln218, Phe220	Phe220: 1
Spike glycoprotein-Open state	6VYB		-6.3	0.0	Thr33, Phe59, Asp287	0
Membrane protein	3I6G		-0.6	0.0	Gly0	0
Envelope small membrane protein	2MM4		-2.2	0.0	Lys63, Asn64	0
Replicase polyprotein 1ab	1Q2W		-7.0	0.0	Phe3, Lys5, Arg131, Trp207, Phe291, Ile286, Asp289	Trp207: 1
Replicase polyprotein 1a	5RE4		-6.7	0.0	Lys137, Thr199, Tyr239, Leu286, Leu287, Glu288, Asp289	Tyr239, Asp289: 3

Protein	PDB ID	Ligand		Energy	RMSD	Residues	H-bond
Protein 7a	1XAK			-5.4	0.0	Tyr3, His47, Arg57, Thr59	0
Protein 9b	2CME			-5.0	0.0	Ser56, Leu65, Glu66, Ala67, Arg68, Ala69, Phe70, Ser72	Ser56: 1
Receptor binding domain of membrane protein	6M17			-6.1	0.0	Cys336, Phe338, Gly339, Ala363, Asp364, Val367, Ser371, Ser373, Phe374,	Ser373: 1
Non-structural protein 7	6M71_C			-5.9	0.0	Lys2, Asp5, Thr9, Thr46, Phe49, Val53, Met52	0
Non-structural protein 8	6M71_B, D			-6.0	0.0	Pro133, Asp134, Tyr135, Trp182, Pro178	Tyr135: 1
Non-structural protein 12	6M71_A			-6.6	0.0	Arg181, Gln184, Asn213	0
Non-structural protein 6	Hypothetical model			-5.6	0.0	Gln8, Lys38, Lys42, Leu44	Lys42: 1
Non-structural Protein 10	Hypothetical model			-6.8	0.0	Ile55, His83, Lys96, Val116	His83:1
Protein 3a	Hypothetical model			-6.3	0.0	Phe28, Val29, Arg68, Ala72, Val90	0
Spike glycoprotein	1wyy	Scutifoliamide A Chemspider ID: 23311285 Source: *Piper scutifolium*		-6.4	0.0	Asn910, Ala940, Thr943, Leu944, Gln947, Asn951, Leu1178, Leu1181, Glu1183	0
Spike glycoprotein-Closed state	6VXX			-5.4	0.0	Leu118, Val120, Phe135, Leu141, Leu241	0
Spike glycoprotein-Open state	6VYB			-6.6	0.0	Phe823, Asn824, Val826, Pro863, Pro1057, His1058	Asn824: 1
Membrane protein	3I6G			-0.7	0.0	Gly0	0

19

Protein	PDB	Ligand			Residues	H-bonds
Envelope small membrane protein	2MM4		-0.8	0.0	Ly63	0
Replicase polyprotein 1ab	1Q2W		-6.9	0.0	Arg4, Lys5 and Phe291 (A chain), Lys 5 (B chain)	1; Lys5 (B chain)
Replicase polyprotein 1a	5RE4		-6.8	0.0	Val212, Arg217, Leu220, Gln256, Ile259, Asp263	0
Protein 7a	1XAK		-5.6	0.0	Gln6, Cys8, Val9, Thr12, Leu16, Lys17	Val9, Lys17: 2
Protein 9b	2CME		-4.4	0.0	Ala58, Arg68, Ala69, Phe70, Ser72	0
Receptor binding domain of membrane protein	6M17		-5.9	0.0	Gln493, Tyr495, Gly502, Tyr505	Gln493, Gly502: 2
Non-structural protein 7	6M71_C		-5.9	0.0	Asp5, Thr9, Thr46, Phe49, Glu50, Val53	Thr9: 1
Non-structural protein 8	6M71_B, D		-6.0	0.0	Leu128, Met129, Pro133, Thr141, Tyr149	0
Non-structural protein 12	6M71_A		-6.1	0.0	Asp484, Ile488, Gln573, Ser578, Ala581	0
Non-structural Protein 6	Hypothetical model		-5.5	0.0	Leu16, Ile17, Arg20, Thr21	Arg20: 1
Non-structural Protein 10	Hypothetical model		-5.6	0.0	His83, Leu92, Asn114, Thr115, Val116	Val116: 2
Protein 3a	Hypothetical model		-5.4	0.0	Cys130, Trp131, His150, His204, His227	0
Spike glycoprotein	1wyy	Tamaridone Pubchem ID: 15345466 Source: *Tamarix dioica*	-7.2	0.0	Asp931, Asn935, Lys1162, Asp1165, Asn1168, Lys1172	1; Asn935
Spike glycoprotein- Closed state	6VXX		-7.3	0.0	Ala520, Phe559, Phe562, Gln563, Gln564, Phe565, Gly566, Arg567	Gln564, Phe565, Arg567: 4

20

Spike glycoprotein-Open state	6VYB	-6.8	0.0	Thr732, Thr778, Ser780, Pro863, His1058	Ser730: 2
Membrane protein	3I6G	-0.8	0.0	Gly0	0
Envelope small membrane protein	2MM4	-3.1	0.0	Lys63, Asn64	Asn64: 1
Replicase polyprotein 1ab	1Q2W	-6.3	0.0	Gly11, Lys12, Glu14, Gly15,	Gly11: 1
Replicase polyprotein 1a	5RE4	-7.0	0.0	Leu87, Lys137, Thr190, Tyr237, Tyr239, Leu285	Tyr237: 1
Protein 7a	1XAK	-5.7	0.0	Val9, Thr12, Val14, Arg65	0
Protein 9b	2CME	-5.6	0.0	Arg68, Gln71, Ser72	0
Receptor binding domain of membrane protein	6M17	-6.5	0.0	Thr345, Arg346, Ser349, Lys441, Lys444, Asn448, Asn450, Tyr451	Lys444: 1
Non-structural protein 7	6M71_C	-5.9	0.0	Lys2, Val6, Thr9, Phe49, Met52	Thr9: 1
Non-structural protein 8	6M71_B, D	-5.7	0.0	Leu128, Val130, Val131, Thr141, Tyr149	0
Non-structural protein 12	6M71_A	-6.7	0.0	Lys47, His133, Asn138, Lys780	0
Non-structural Protein 6	Hypothetical model	-5.6	0.0	Lys48, Ser50, Leu52, Asp53, Gln56	Leu52: 1
Non-structural Protein 10	Hypothetical model	-6.7	0.0	Pro37, Asn105, Asp106, Phe110, Lys113, Asn114, Tyr126	Asn105, Asn114: 2
Protein 3a	Hypothetical model	-6.6	0.0	Gln213, Val255, Ile263, Thr270	0

370

21

371   Hyoscyamine ([(1S,5R)-8-methyl-8-azabicyclo [3.2.1] octan-3-yl] (2S)-3-hydroxy-2-phenyl-

372   propanoate), an alkaloid derivative and anticholinergic, derived from *Datura stramonium*

373   (Jimson weed) is known to inhibit receptors in smooth and cardiac muscle, the sino-atrial and

374   atrio-ventricular node for a slow ventricular response during atrial fibrillation [74,75]. The

375   molecular docking studies suggested that Hyoscyamine showed good binding potential

376   towards the spike glycoprotein in the post-fusion, closed state, and open state conformations

377   with the binding energies of -8.14, -6.0, and -5.7 kcal/mol, respectively. The interacting

378   residues present in the binding cavity of post-fusion conformation of spike protein were

379   identified to be Ser924, Thr925, Gly928, Asp932, Gln1161, ILe1164, Asn1168 (Chain A)

380   and Ser924, Thr925, Gly928, Gln1161, Ile1164 (Chain B). The interaction stabilized by two

381   hydrogen bonds with Asn1168 of Chain A (**Fig. 4a**). It was observed that these residues

382   located at one of the binding sites as predicted by the Castp and Depth servers. Similarly,

383   Trp104, Ile119, Val126, Ile128, Tyr170, Ser172, Ile203, and Val227 were identified to be the

384   major residues in the binding site of the open state conformation of spike protein, and the

385   interaction stabilized by a hydrogen bond (**Fig. 4b**). The main interacting residues at the

386   binding site of the closed state conformation were identified to be Leu335, Pro337, Phe338,

387   Gly339, Asp364, and Val367 (**Fig. 4c**). Thus, it is clear that the conformations play a vital

388   role in the binding of the ligand, and maximum interactions were observed between the post-

389   fusion conformation of the spike glycoprotein and the lead molecule in comparison with

390   other conformations. The binding energy of the docked complex of Hyoscyamine and

391   replicase polyprotein 1a was estimated to be -6.1 kcal/mol, and the interacting residues were

392   Glu156, Met165, Asp187, Arg188, Gln189, and Gln192 along with a hydrogen bond (**Fig.

393   4d**). Similarly, the lead molecule showed binding energy of -5.4 kcal/ mol towards the RBD

394   of the membrane protein. The main interacting residues present in the binding cavity were

395   found to be Thr376, Val407, Ala411, Val433, and Tyr508 (**Fig. 4e**). Hyoscyamine showed

396   binding energy of -0.7 kcal/mol (interacting residue: Gly) towards membrane protein (**Fig.

397   4f**), and the lead molecule exhibited the binding energy of -2.2 kcal/mol towards the envelope

398   protein. Lys63 and Asn64 were found to be the main interacting residues (**Fig.4g**). The

399   binding energy of the docked complex of replicase polyprotein1a and Hyoscyamine was

400   estimated to be -6.0 kcal/mol. The main interacting residues were found to be Trp218,

401   Asn221 and Leu271, which formed a hydrogen bond (**Fig.4h**). The binding energies of the

402   docked complexes of Protein 3a, 7a, and 9b and ligand were estimated to be -5.3, -4.4, and -

403   4.4 kcal/mol, respectively. The interacting residues of protein 3a included Phe56, Ile63,

404   Lys66, Tyr189, and Glu191 **(Fig. 4i)**. Similarly, interacting residues of protein 7a included

405   Tyr3, Tyr5, His47, Gln61 **(Fig. 4j)**, and the residues present in the binding cavity of protein

406   9b were found to be Arg68, Ala69, and Phe70 **(Fig. 4k)**. The binding energies of ligand and

407   nsp7, nsp8, and nsp12 of RdRp were estimated to be -5.3, -5.9, and -5.4 kcal/mol,

408   respectively. The nsp7 interacted with the lead molecule via Thr46, Phe49, and Val53 **(Fig.**

409   **4l)**. Similarly, the interacting residues present at the binding site of nsp8 were observed to be

410   Leu128, Val130, Thr141, and Tyr149 **(Fig. 4m)**, and the interacting residues present in the

411   binding pocket of nsp12 were found to be Phe412, Phe415, Phe440, and Phe843 **(Fig. 4n)**.

412   The binding energy associated with the interaction between ligand and non-structural protein

413   6, and 10 were estimated to be -5.2 and -6.1 kcal/mol, respectively. The interacting residues

414   present at the binding site were identified to be Asp6, Phe7, Leu15, Leu40, and Ile60 **(Fig.**

415   **4o)**. Similarly, the interacting residues present in the binding pocket of non-structural protein

416   10 were identified to be Ile55, Cys74, Tyr76, His83, Asp91, Leu112, Thr115, and Val116

417   along with a hydrogen bond **(Fig. 4p)**. Thus, the interaction modeling of natural lead

418   Hyoscyamine towards the selected targets of SARS-CoV-2 suggested that the highest binding

419   potential observed towards the spike glycoprotein in the post-fusion conformation with a

420   binding energy of -8.14 kcal/mol, and several stabilizing interactions were observed in

421   comparison with other selected molecular targets.

422

Fig. 4. Prediction of the binding potential of Hyoscyamine towards the prioritized molecular targets of SARS-CoV by molecular docking visualized in MGL tools of AutoDock. The figure displayed the binding pocket of the ligand-receptor complex. The interacting residues and the ligands are displayed in stick figures. The interacting residues and binding energy are labeled (a) Binding of the ligand and post-fusion conformation of spike glycoprotein (binding energy: -8.14 kcal/mol) (b) Binding of the ligand and open state spike glycoprotein (binding energy: -6.0 kcal/mol) (c) Binding of the ligand and closed state spike glycoprotein (binding energy -5.7 kcal/mol) (d) Binding of the ligand and replicase polyprotein 1ab (binding energy: -6.1 kcal/mol) (e) Binding of the ligand and receptor binding domain of membrane protein (binding energy: -5.4 kcal/mol) (f) Binding of the ligand and membrane protein (binding energy: -0.7 kcal/mol) (g) Binding of the ligand and small envelope protein (binding energy: -2.2 kcal/mol) (h) Binding of the ligand and replicase polyprotein 1a (binding energy: -6.0 kcal/mol) (i) Binding of the ligand and protein3a (binding energy: -6.1 kcal/mol) (j) Binding of the ligand and protein7a (binding energy: -4.4 kcal/mol) (k) Binding of the ligand and protein 9b (binding energy: -4.4 kcal/mol) (l) Binding of the ligand and non-structural protein7 (binding energy: -5.3 kcal/mol) (m) Binding of the ligand and non-structural protein 8 (binding energy: -5.9 kcal/mol) (n) Binding of the ligand and non-structural protein12 (binding energy: -5.4 kcal/mol) (o) Binding of the ligand and non-structural protein 6 (binding energy: -5.2 kcal/mol) (p) Binding of the ligand and non-structural protein 10 (binding energy: -6.1 kcal/mol)

Rotiorinol-C ((9R,9aR)-3-acetyl-9-hydroxy-6-[(1E,3E,5S)-7-hydroxy-3,5-dimethylhepta-1,3-dienyl]-9a-methyl-9H-furo [3,2-g] isochromen-2-one), an azaphilone derived from the fungus *Chaetomium cupreum* (Dark-walled mold), which is known to exhibit antimicrobial activities [76]. Rotiorinol-C showed the binding potential to the spike glycoprotein in the post-fusion, closed state, and open state conformations with the binding energies of -6.5, -6.2, and -6.3 kcal/mol, respectively. The main residues present in post-fusion conformation were included Gln931, Asn936, Asn942, Val1157, Asn1159, Gln1161, Asn1168, and Lys1172, and the interaction stabilized by two hydrogen bonds **(Fig. 5a)**. The interacting residues present in the closed state conformation were observed to be Arg34, Thr208, Pro209, Leu212, Pro217, Gln218, and Phe220. The lead molecule interacted with Phe220 by a hydrogen bond **(Fig. 5b)**. Similarly, the major interacting residues present at the binding site of the open state conformation of spike glycoprotein were identified to be Thr33, Phe59, and Asp287 **(Fig. 5c)**. Rotiorinol-C showed higher interaction with the post-fusion conformation of the spike glycoprotein when compared to the open and closed state conformations. The binding energy of the docked complex of replicase polyprotein 1ab and the lead molecules were estimated to be -9.82 kcal/mol, and the major residues involved in the binding were observed to be Arg4, Lys5, Tyr126, Gln127, Arg131, Asp289, and Glu290. The interactions were stabilized by five hydrogen bonds **(Fig. 5d)**. The interaction of lead and receptor-binding domain of the membrane protein showed the binding energy of -6.1 kcal/mol, and the major residues involved in the binding were observed to be Cys336, Phe338, Gly339, Ala363, Asp364, Val367, Ser371, Ser373, and Phe374. A hydrogen bond formed between the ligand and Ser373 of the receptor-binding domain **(Fig. 5e)**. The docked complexes were demonstrated the binding energies of -0.6 and -2.2 kcal/mol towards the membrane protein **(Fig. 5f)** and envelope protein **(Fig. 5g)**, respectively. The binding energy of the docked complex of ligand and replicase polyprotein1a was estimated to be -6.7 kcal/mol. The major interacting residues involved in the interaction were found to be Lys137, Thr199, Tyr239, Leu286, Leu287, Glu288, and Asp289. The interactions were stabilized by three hydrogen bonds **(Fig. 5h)**. The binding energies associated with the interaction of lead molecule and Protein 3a, 7a, and 9b were estimated to be -6.3, -5.4, and -5.0 kcal/mol, respectively. The major interacting residues present at the binding site of protein 3a were identified to be Phe28, Val29, Arg68, Ala72, and Val90 **(Fig. 5i)**. The major interacting residues present in the protein 7a were identified to be Tyr3, His47, Arg57, Thr59 **(Fig.5j)**, and the main interacting residues present in protein 9b were included Ser56, Leu65, Glu66, Ala67, Arg68, Ala69, Phe70, and Ser72,

478 and the interaction stabilized by a hydrogen bond **(Fig. 5k)**. The binding energies of the

479 docked complexes of lead molecules and nsp7, nsp8, and nsp12 of RdRp were estimated to

480 be -5.9, -6.0, and -6.6 kcal/mol, respectively. The major residues that interacted with nsp7

481 were identified to be Lys2, Asp5, Thr9, Thr46, Phe49, Met52, and Val53 **(Fig. 5l)**. Similarly,

482 the main residues that interacted with nsp8 were found to be Pro133, Asp134, Tyr135,

483 Trp182, and Pro178. The interaction stabilized by a hydrogen bond (Tyr135) **(Fig. 5m)**. The

484 major interacting residues present at the binding site of nsp12 were found to be Arg181,

485 Gln184, and Asn213 **(Fig. 5n)**. The binding energies associated with the docked complex of

486 lead molecules and non-structural proteins 6 and 10 and were estimated to be -5.6 and -6.8

487 kcal/mol, respectively. The major interacting residues present in the non-structural protein 6

488 were observed to be Gln8, Lys38, Lys42, and Leu44. The interaction stabilized by a

489 hydrogen bond **(Fig. 5o)**. Similarly, the main interacting residues present in the non-structural

490 protein10 were identified to be Ile55, His83, Lys96, and Val116. The interaction stabilized by

491 a hydrogen bond **(Fig. 5p)**. From the interaction modeling, it is clear that Rotiorinol-C

492 showed greater binding potential towards the replicase polyprotein (binding energy: -9.82

493 kcal/mol) when compared to the binding energies of the interaction between the ligand and

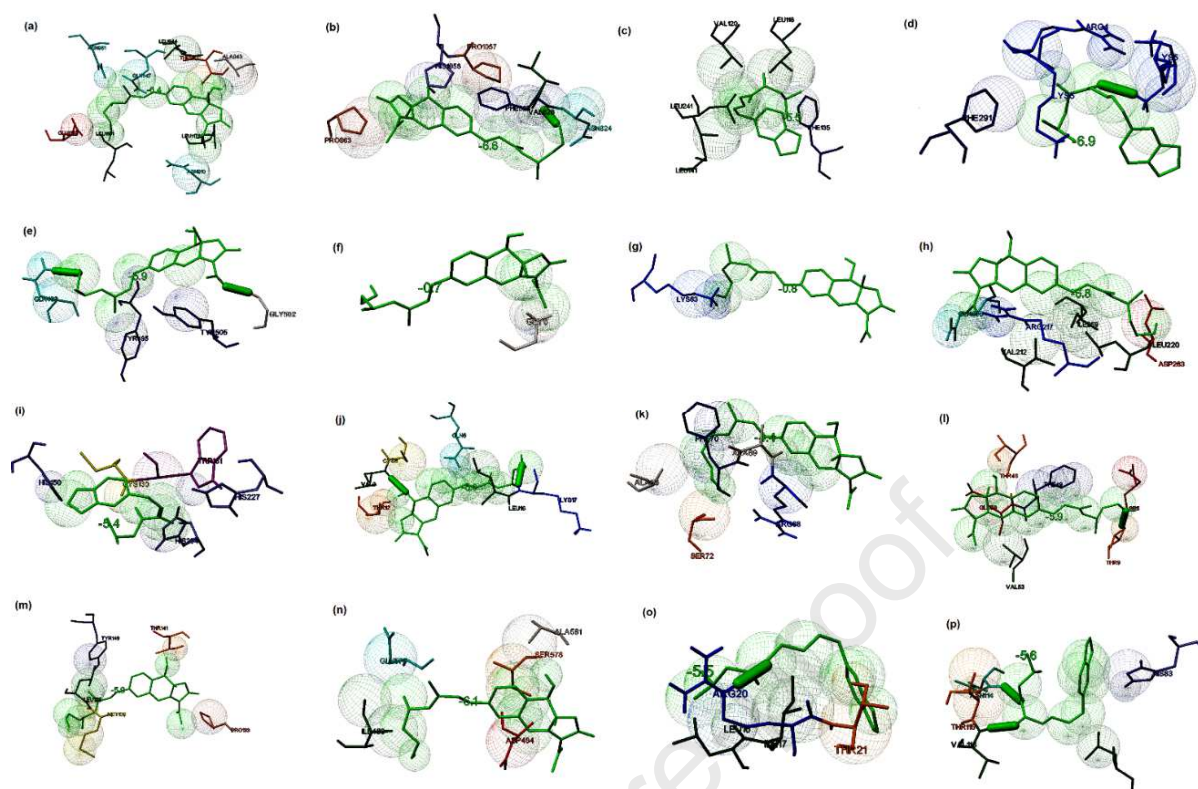494 other prioritized targets of SARS-CoV-2.

495

496

26

Fig. 5. Prediction of the binding potential of Rotiorinol-C towards the prioritized molecular targets of SARS-CoV by molecular docking visualized in MGL tools of AutoDock. The figure displayed the binding pocket of the ligand-receptor complex. The interacting residues and the ligands are displayed in stick figures. The interacting residues and binding energy are labeled (a) Binding of the ligand and post-fusion conformation of spike glycoprotein (binding energy: -6.5 kcal/mol) (b) Binding of the ligand and open state spike glycoprotein (binding energy: -6.3 kcal/mol) (c) Binding of the ligand and closed state spike glycoprotein (binding energy -6.2 kcal/mol) (d) Binding of the ligand and replicase polyprotein 1ab (binding energy: -9.8 kcal/mol) (e) Binding of the ligand and receptor binding domain of membrane protein (binding energy: -6.1 kcal/mol) (f) Binding of the ligand and membrane protein (binding energy: -0.6 kcal/mol) (g) Binding of the ligand and small envelope protein (binding energy: -2.2 kcal/mol) (h) Binding of the ligand and replicase polyprotein 1a (binding energy: -6.7 kcal/mol) (i) Binding of the ligand and protein3a (binding energy: -6.3 kcal/mol) (j) Binding of the ligand and protein7a (binding energy: -5.4 kcal/mol) (k) Binding of the ligand and protein 9b (binding energy: -5.0 kcal/mol) (l) Binding of the ligand and non-structural protein7 (binding energy: -5.3 kcal/mol) (m) Binding of the ligand and non-structural protein 8 (binding energy: -5.9 kcal/mol) (n) Binding of the ligand and non-structural protein12 (binding energy: -6.6 kcal/mol) (o) Binding of the ligand and non-structural protein 6 (binding energy: -5.6 kcal/mol) (p) Binding of the ligand and non-structural protein 10 (binding energy: -6.8 kcal/mol)

Scutifoliamide-A ((2E, 4Z)-5-(1, 3-Benzodioxol-5-yl)-N-isobutyl-2, 4-pentadienamide) is commonly present in *Piper scutifolium* (Pepper) [77]. It showed the binding potential to the spike glycoprotein in the post-fusion, closed state, and open state conformations with the binding energies of -6.4, -5.4, and -6.6 kcal/mol, respectively. The residues present at the binding cavity of the post-fusion conformation were identified to be Asn910, Ala940, Thr943, Leu944, Gln947, Asn951, Leu1178, Leu1181, and Glu1183 **(Fig. 6a)**. The interacting residues present in the binding site of the closed state conformation were observed to be Leu118, Val120, Phe135, Leu141, and Leu241 **(Fig. 6b)**. Similarly, the main interacting residues present in the binding cavity of open state conformation were found to be Phe823, Asn824, Val826, Pro863, Pro1057, and His1058. The interaction stabilized by a hydrogen bond **(Fig. 6c)**. The binding energy of the docked complex of the lead molecule and replicase polyprotein 1ab were identified to be -6.9 kcal/mol, and the main interacting residues were identified to be Arg4, Lys5, and Phe291 (A chain), Lys 5 (B chain) **(Fig. 6d)**. The binding energy of the docked complex of the ligand and the receptor-binding domain of the membrane protein was estimated to be -5.9 kcal/mol. The major residues that interacted with the ligand were identified to be Gln493, Tyr495, Gly502, and Tyr505. The interaction stabilized by hydrogen bonds with Gln493 and Gly502 **(Fig. 6e)**. The binding energies associated with the docked complexes of the ligand and membrane protein, and ligand and envelope protein were estimated to be -0.7 **(Fig. 6f)** and -0.8 kcal/mol **(Fig. 6g)**, respectively.

The binding energy associated with the complex of the lead molecule and replicase polyprotein1a was identified to be -6.8 kcal/mol, and the main interacting residues at the binding cavity were identified to be Val212, Arg217, Leu220, Gln256, Ile259, and Asp263 **(Fig. 6h)**. The binding energies associated with the docked complex of ligand and Protein 3a, 7a and 9b were estimated to be -5.4, -5.6, and -4.4 kcal/mol, respectively. The main interacting residues present at the binding site of protein 3a were identified to be Cys130, Trp131, His150, His204, and His227. The interaction stabilized by a hydrogen bond **(Fig. 6i)**. Similarly, the major interacting residues present at the binding site of protein 7a were found to be Gln6, Cys8, Val9, Thr12, Leu16, and Lys17. The interaction stabilized by two hydrogen bonds **(Fig. 6j).** The major binding residues present in the protein 9b were included Ala58, Arg68, Ala69, Phe70, and Ser72 **(Fig. 6k)**. The binding energies of the docked complex of ligand and nsp7, nsp8, and nsp12 were estimated to be -5.9, -6.0, and -6.1 kcal/mol, respectively. The main residues present at the binding site of nsp7 included Asp5, Thr9, Thr46, Phe49, Glu50, and Val53. The interaction stabilized by a hydrogen bond **(Fig. 6l)**. The residues present at the binding site of nsp8 were found to be Leu128, Met129, Pro133, Thr141, and Tyr149 **(Fig. 6m)**. The main amino acid residues present at the binding site of nsp12 were identified to be Asp484, Ile488, Gln573, Ser578, and Ala581 **(Fig. 6n)**. The binding energies associated with the docked complexes of the ligand and non-structural proteins 6 and 10 were estimated to be -5.5 and -5.6 kcal/mol, respectively. The interacting residues present in the non-structural protein 6 were observed to be Leu16, Ile17, Arg20, and Thr21, and the interaction stabilized by a hydrogen bond with Arg20 **(Fig. 6o)**. Similarly, the major interacting residues present in the non-structural protein10 were included His83, Leu92, Asn114, Thr115, and Val116. The interaction stabilized by two hydrogen bonds **(Fig. 6p)**. The computational modeling suggested that Scutifoliamide-A showed the profound binding potential to several prioritized targets, which showed the highest binding energy to replicase polyprotein 1ab (-6.9 kcal/mol) when compared to the binding energy of the interaction between Scutifoliamide-A and other selected targets of SARS-CoV-2.

28

Fig. 6. Prediction of the binding potential of Scutifoliamide-A towards the prioritized molecular targets of SARS-CoV by molecular docking visualized in MGL tools of AutoDock. The figure displayed the binding pocket of the ligand-receptor complex. The interacting residues and the ligands are displayed in stick figures. The interacting residues and binding energy are labeled (a) Binding of the ligand and post-fusion conformation of spike glycoprotein (binding energy: -6.4 kcal/mol) (b) Binding of the ligand and open state spike glycoprotein (binding energy: -6.6 kcal/mol) (c) Binding of the ligand and closed state spike glycoprotein (binding energy -5.4 kcal/mol) (d) Binding of the ligand and replicase polyprotein 1ab (binding energy: -6.9 kcal/mol) (e) Binding of the ligand and receptor binding domain of membrane protein (binding energy: -5.9 kcal/mol) (f) Binding of the ligand and membrane protein (binding energy: -0.7 kcal/mol) (g) Binding of the ligand and small envelope protein (binding energy: -0.8 kcal/mol) (h) Binding of the ligand and replicase polyprotein 1a (binding energy: -6.8 kcal/mol) (i) Binding of the ligand and protein3a (binding energy: -5.4 kcal/mol) (j) Binding of the ligand and protein7a (binding energy: -5.6 kcal/mol) (k) Binding of the ligand and protein 9b (binding energy: -4.4 kcal/mol) (l) Binding of the ligand and non-structural protein7 (binding energy: -5.9 kcal/mol) (m) Binding of the ligand and non-structural protein 8 (binding energy: -6.0 kcal/mol) (n) Binding of the ligand and non-structural protein12 (binding energy: -6.1 kcal/mol) (o) Binding of the ligand and non-structural protein 6 (binding energy: -5.5 kcal/mol) (p) Binding of the ligand and non-structural protein 10 (binding energy: -5.6 kcal/mol)

Tamaridone (5,7-dihydroxy-2-(2-hydroxy-4-methoxyphenyl)-6-methoxychromen-4-one), a flavone present in *Tamarix dioica* (Lal jhau / Ban jhau) showed binding potential towards the spike glycoprotein in the post-fusion, closed state, and open state conformations with the binding energies of -7.2, -7.3 and -6.8 kcal/mol, respectively. The interacting residues present

591 in the binding pocket of the post-fusion conformation of spike protein were found to be

592 Asp931, Asn935, Lys1162, Asp1165, Asn1168, and Lys1172 **(Fig.7a)**. The interacting

593 residues at the binding pocket of the closed state were identified to be Ala520, Phe559,

594 Phe562, Gln563, Gln564, Phe565, Gly566, and Arg567. The interaction stabilized by four

595 hydrogen bonds **(Fig. 7b)**. Similarly, the major residues present in the binding site of the

596 open state conformation were identified to be Thr732, Thr778, Ser780, His1058 and Pro863.

597 The interaction stabilized by a hydrogen bond **(Fig. 7c)**. The binding energy of the docked

598 complex of the lead molecule and replicase polyprotein 1ab was estimated to be -6.3

599 kcal/mol. The main residues involved in the interactions were predicted to be Gly11, Lys12,

600 Glu14, and Gly15. The interaction stabilized by a hydrogen bond **(Fig. 7d)**. The binding

601 energy associated with the complex of ligand and receptor-binding domain of the membrane

602 protein was estimated to be -6.5 kcal/mol, and the major interacting residues were identified

603 to be Thr345, Arg346, Ser349, Lys441, Lys444, Asn448, Asn450, and Tyr451. The

604 interaction stabilized by a hydrogen bond **(Fig. 7e)**. The docked complexes of ligand-

605 membrane protein and ligand- envelope protein showed binding energies of -0.8 **(Fig. 7f)** and

606 -3.1 kcal/mol **(Fig. 7g)**, respectively. The binding energy of the docked complex of the lead

607 molecule and replicase polyprotein 1a was estimated to be -7.0 kcal/mol. The major

608 interacting residues present in the binding site of replicase polyprotein 1a were found to be

609 Leu87, Lys137, Thr190, Tyr237, Tyr239, and Leu285. The interaction stabilized by a

610 hydrogen bond **(Fig. 7h)**. The binding energies associated with the interaction of ligand and

611 protein 3a, 7a, and 9b were estimated to be -6.6, -5.7 and -5.6 kcal/mol, respectively. The

612 main interacting residues present in protein3a were identified to be Gln213, Ile263, Val255,

613 and Thr270 **(Fig.7i)**. Similarly, the major interacting residues present at the binding site of

614 protein 7a were included Val9, Thr12, Val14, and Arg65 **(Fig. 7j).** The main amino acids that

615 interacted with protein9b were identified to be Arg68, Gln71, and Ser72 **(Fig. 7k)**. The

616 binding energies of the docked complexes of nsp7, nsp8, and nsp12 of RdRp were estimated

617 to be -5.9, -5.7, and -6.7 kcal/mol, respectively. The major residues at the binding site of nsp7

618 were found to be Lys2, Val6, Thr9, Phe49, Met52 with a hydrogen bond formation **(Fig. 7l)**.

619 Similarly, the main interacting residues present in nsp8 were found to be Leu128, Val130,

620 Val131, Thr141, and Tyr149 **(Fig. 7m)**. The major interacting residues present in nsp12 were

621 found to be Lys47, His133, Asn138, and Lys780 **(Fig. 7n)**. The binding energies associated

622 with the ligand and non-structural proteins 6, and 10 were estimated to be -5.7 and -6.7

623 kcal/mol, respectively. The major interacting residues present in the non-structural protein6

624 were observed to be Lys48, Ser50, Leu52, Asp53, and Gln56. The interaction stabilized by

625 two hydrogen bonds **(Fig. 7o)**. Similarly, the major interacting amino acids present in non-

626 structural protein 10 were identified to be Pro37, Asn105, Asp106, Phe110, Lys113, Asn114,

627 and Tyr126. The interaction stabilized by two hydrogen bonds **(Fig.7p)**. Thus, the interaction

628 modeling of Tamaridone and fourteen prioritized targets of SARS-CoV-2 suggested that the

629 lead showed the highest binding potential to the spike glycoprotein (binding energy: -7.2

630 kcal/mol) when compared to the binding energies associated with the interaction between

631 ligands and other selected targets.

632

633

634

635 **Fig. 7**. Prediction of the binding potential of Tamaridone towards the prioritized molecular
636 targets of SARS-CoV by molecular docking visualized in MGL tools of AutoDock. The
637 figure displayed the binding pocket of the ligand-receptor complex. The interacting residues
638 and the ligands are displayed in stick figures. The interacting residues and binding energy are
639 labeled (a) Binding of the ligand and post-fusion conformation of spike glycoprotein (binding
640 energy: -7.2 kcal/mol) (b) Binding of the ligand and open state spike glycoprotein (binding

31

energy: -7.3 kcal/mol) (c) Binding of the ligand and closed state spike glycoprotein (binding energy -6.8 kcal/mol) (d) Binding of the ligand and replicase polyprotein 1ab (binding energy: -6.3 kcal/mol) (e) Binding of the ligand and receptor-binding domain of membrane protein (binding energy: -6.5 kcal/mol) (f) Binding of the ligand and membrane protein (binding energy: -0.8 kcal/mol) (g) Binding of the ligand and small envelope protein (binding energy: -3.1 kcal/mol) (h) Binding of the ligand and replicase polyprotein 1a (binding energy: -7.0 kcal/mol) (i) Binding of the ligand and protein3a (binding energy: -6.6 kcal/mol) (j) Binding of the ligand and protein7a (binding energy: -5.7 kcal/mol) (k) Binding of the ligand and protein 9b (binding energy: -5.6 kcal/mol) (l) Binding of the ligand and non-structural protein7 (binding energy: -5.9 kcal/mol) (m) Binding of the ligand and non-structural protein 8 (binding energy: -6.0 kcal/mol) (n) Binding of the ligand and non-structural protein12 (binding energy: -6.7 kcal/mol) (o) Binding of the ligand and non-structural protein 6 (binding energy: -5.6 kcal/mol) (p) Binding of the ligand and non-structural protein 10 (binding energy: -6.7 kcal/mol

Similarly, the interaction between two currently suggested drugs against COVID-19 and their usual targets were predicted by molecular docking studies. The binding energies associated with the interaction between Chloroquine and Hydroxychloroquine to their normal drug targets namely glutathione S transferase of *Plasmodium falciparum* and human angiotensin-converting enzyme 2 (hACE2), respectively, were predicted by molecular docking. The interaction modeling suggested that when Chloroquine docked with glutathione S transferase, the complex showed binding energy of -3.71 kcal/mol. The main interacting residues were identified to be Glu90, Leu91, Glu93, Phe94, and Asp97 **(Fig. 8a & b)**. The number of interacting residues at the binding pockets was less when compared to the interaction of natural molecules and the selected targets selected. When Hydroxychloroquine docked with human angiotensin-converting enzyme 2 (hACE2), the docked conformation showed binding energy of -1.0 kcal/mol. The complex showed that Gln287 interacted with the ligand **(Fig. 8c & d)** and no hydrogen bonds were involved in the interaction. From the molecular docking studies, it is clear that the natural lead molecules showed better binding to the selected molecular targets based on binding energy (kcal/mol), the number of hydrogen bonds and other weak interactions, and the number of amino acids involved in the binding when compared to the binding of Chloroquine and Hydroxychloroquine and their usual targets.

674

Fig. 8. Prediction of the binding of conventional antiviral drugs towards their usual drug targets by molecular docking studies (a) Interaction of Chloroquine with its usual targets glutathione S transferase of Plasmodium falciparum (b) Binding affinity of Chloroquine towards glutathione S transferase (binding energy: -3.7 kcal/mol) illustrated the major residues involved in the interaction with the ligand (c) Interaction of Hydroxy-chloroquine with usual target human angiotensin-converting enzyme 2 (hACE2) (d) Binding affinity of Hydroxyl-chloroquine towards hACE2 (binding energy:-1.0 kcal/mol) illustrated the major residues involved in the interaction with the ligand.

683

684 3.5. Molecular dynamic simulation studies

685 Four potential docked complexes with the minimum binding energy (kcal/mol), cluster RMS,

686 and a greater number of stabilizing interactions were selected for MD simulation studies. The

687 best-docked conformations of spike glycoprotein and Hyoscyamine, replicase polyprotein

688 1ab and Rotiorinol-C, replicase polyprotein 1ab and Scutifoliamide A, Spike glycoprotein,

689 and Tamaridone were simulated at 100 ns using NVT ensemble to confirm the dynamics and

690 stabilities during the binding. Similarly, the docked complex of Chloroquine and glutathione-

691 S-transferase were simulated, and their binding stabilities were compared with the interaction

692 stabilities of the docked complexes of natural lead molecules and selected targets.

693

694 The trajectories obtained during the MD simulation of the best-docked pose of Hyoscyamine

695 and the post-fusion conformation of the spike glycoprotein complex are shown in **Fig. 9**. The

696 MD simulation studies suggested that the RMSD value of the protein showed a deviation

33

697   from 8 to 16 Å at100ns, which indicated that there were substantial changes in the

698   conformation of the target protein during the simulation period **(Fig. 9a)**. The variation in the

699   RMSD probably due to the binding of Hyoscyamine with the protein, which indicated better

700   interaction and stability when compared to the control. The protein RMSF deviated from 2.0-

701   14.0Å and showed that more than 60% of the residues possessed >10Å. The fluctuations in

702   the protein with the C- and N-terminals are depicted in **Fig. 9b**. The ligand RMSF ranged

703   from 4.0-6.0Å, indicated that the fluctuations in their entropic role, and the interactions with

704   the target during the binding are shown in **Fig. 9c**. The protein-ligand interactions throughout

705   the simulation time showed prominent water bridges, hydrogen bonds, and hydrophobic

706   interactions (**Fig. 9d)**. The molecular interactions that occurred during more than 10% of the

707   simulation period are illustrated in **Fig. 9e**. The simulation studies revealed that the ligand

708   binds to the protein with hydrophobic interaction with Ile1164 of chain B and a polar

709   interaction with Gln1161 of chain A. The interactions between the ligand and the protein are

710   shown in **Fig. 9f**. The trajectories of total contacts between the ligand and target such as

711   hydrogen bonds, ionic bonds, water bridges, and hydrophobic interactions were found to be

712   constant throughout the simulation. It was found that several residues interacted with the

713   ligand throughout the trajectory frame in which several residues belonged to chain A and

714   chain B, which indicated binding stabilities during the simulation. The conformational

715   changes of protein and ligand that occurred during the MD simulation are shown in

716   Supplementary Materials Fig. S1. Thus, the MD simulation studies suggested that the

717   stabilities of the interaction between Hyoscyamine and spike glycoprotein of SARS-CoV-2

718   were better when compared to the stability of the docked complex of chloroquine and its

719   usual target **(Fig. 13)**. Thus, the present study suggested that Hyoscyamine can act as a

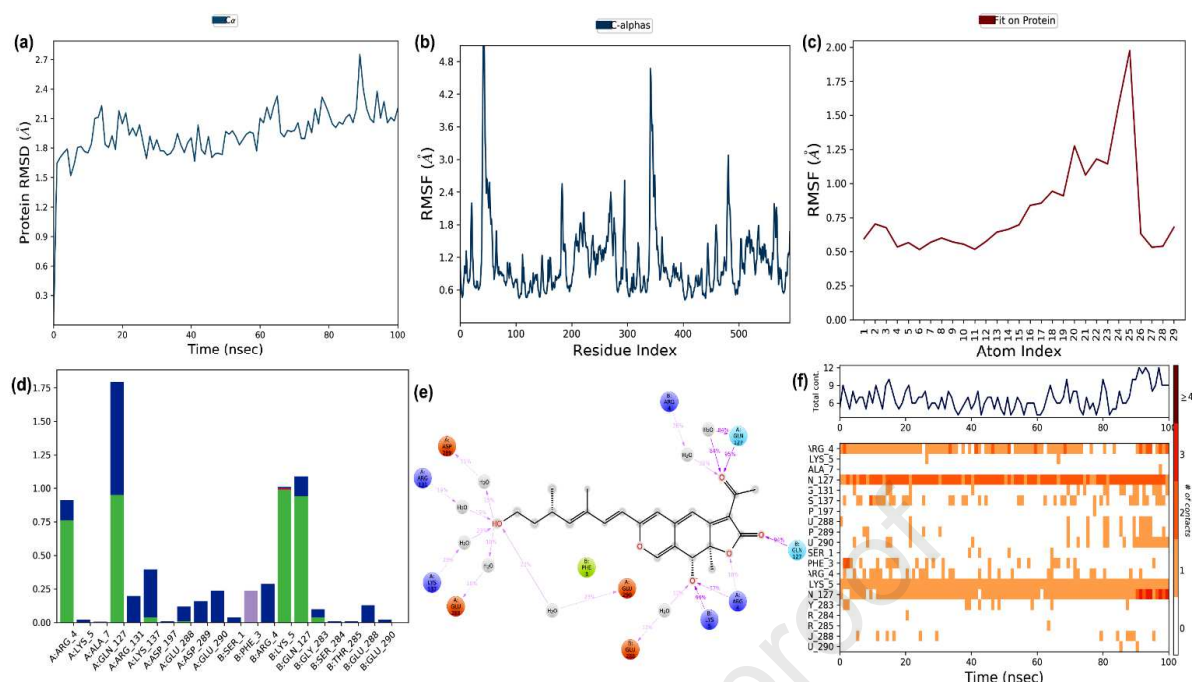720   potential lead molecule against the spike glycoprotein of SARS-CoV-2.

34

Fig. 9. The binding and stability of the docked complex of natural lead molecule Hyoscyamine and spike glycoprotein of SARS-CoV-2 were studied by molecular dynamic simulation at 100 ns. The trajectories obtained during the MD simulation is shown in figure (a) Protein-ligand RMSD: Protein RMSD (Å) is shown on the y-axis, and simulation time is given on the x-axis (b) Plot of the protein RMSF: RMSF (Å) is given in the y-axis and atom index is showed in the x-axis (c) Plot of ligand RMSF: RMSF (Å) is shown in y-axis and atom index is given in the x-axis (d) The protein-ligand contact is shown in the form of a histogram. The blue, grey, pink, and green regions in the histogram represent water bridges, hydrophobic interactions, ionic bonds, and hydrogen bonds respectively (e) The interactions between Hyoscyamine and post-fusion conformation of the spike glycoprotein observed during MD simulation (f) The protein-ligand contacts shown in the form of timeline representation. The top panel shows the total number of specific contacts between receptor

35

734 and ligand, and the bottom panel shows the amino acid residues of the target, which is
735 interacted with the ligand.
736

737 The MD simulation trajectories of Rotiorinol-C and the replicase polyprotein 1ab are
738 depicted in **Fig. 10**. The simulation studies suggested that the target protein showed RMS
739 deviation from 1.8 to 2.7 Å during the simulation at 100 ns **(Fig.10a)**. This variation in
740 RMSD probably due to the binding of Rotiorinol-C to the protein target. The protein RMSF
741 deviated from 0.6 to 4.8 Å (the majority of the residues deviated from 1.2 to 2.8 Å, and 40%
742 of the residues deviated at 3.6 Å) indicated the fluctuations in the protein structure during the
743 simulation period **(Fig. 10b)**. Similarly, ligand RMSF observed to be fluctuated between 0.5
744 – 2.0 Å due to the variation in entropy caused by the receptor-ligand interaction **(Fig. 10c)**.
745 The protein-ligand interaction throughout the simulation is shown in **Fig. 10c,** which depicted
746 that hydrogen and hydrophobic interactions played major roles in the binding. The interaction
747 that occurred during more than 10% of the simulation time is shown in **Fig. 10d**. The ligand
748 interacted to the protein with Phe3 of chain B, electrostatic negative interactions with
749 Glu288, Asp289, Glu290 of chain A and Glu288 of chain B, electrostatic interactions with
750 Arg4, Arg131, Lys137 of chain A and Arg4, Lys5 of chain B, polar interactions with Gln127
751 of both the chains. The interactions between the ligand and the protein are shown in **Fig. 10f**.
752 The trajectory forces such as hydrogen bonds, ionic bonds, water bridges, and hydrophobic
753 interactions during the simulation were evident. The interaction contacts were observed to be
754 constant up to 80ns with a minor increase, and several amino acids interacted with the ligand
755 throughout the trajectory frame. Arg4, Gln127 of chain A and Lys5, Gln127 of chain B were
756 showed constant interaction with the ligand throughout the simulation. The structural changes
757 associated with the protein and ligand during the MD simulation are shown in Supplementary
758 Materials Fig. S2. Thus, the MD simulation suggested that the stability of the interaction
759 between Rotiorinol-C and replicase polyprotein 1ab were greater when compared to the
760 interaction of chloroquine and its usual target. Thus, this study revealed that Rotiorinol-C can
761 act as one of the potential lead molecules towards replicase polyprotein 1ab of SARS-CoV-2.
762

763

Fig. 10. The binding and stability of the docked complex of natural lead molecule Rotiorinol-C and replicase polyprotein 1ab of SARS-CoV-2 studied by molecular dynamic simulation at 100 ns. The trajectories obtained during the MD simulation is shown in figure (a) Protein-ligand RMSD: Protein RMSD (Å) is shown on the y-axis, and simulation time is given on the x-axis (b) Plot of the protein RMSF: RMSF (Å) is given in the y-axis and atom index is showed in the x-axis (c) Plot of ligand RMSF: RMSF (Å) is shown in y-axis and atom index is given in the x-axis (d) The protein-ligand contact is shown in the form of a histogram. The blue, grey, pink, and green regions in the histogram represent water bridges, hydrophobic interactions, ionic bonds, and hydrogen bonds respectively (e) The interactions between Hyoscyamine and post-fusion conformation of the spike glycoprotein observed during MD simulation (f) The protein-ligand contacts shown in the form of timeline representation. The top panel shows the total number of specific contacts between receptor and ligand, and the bottom panel shows the amino acid residues of the target, which is interacted with the ligand.

777

The simulation trajectories of the interaction between Scutifoliamide-A and replicase polyprotein 1ab of SARS-CoV-2 are shown in **Fig. 11**. The RMS trajectories suggested that the protein showed a substantial deviation from 5.0 to 45.0 Å at100 ns, which indicated the conformational changes in the target protein **(Fig. 11a)**. The variation in RMSD of the protein was probably due to the interaction of Scutifoliamide-A and the target. The RMSF of the protein was found to be 4.0-28.0Å, in which more than 40% of the residues showed >20Å **(Fig. 11b)**. The ligand RMSF ranged between10.0-25.0Å indicated that the fluctuations corresponding to their variations in entropy due to the interaction with the target **(Fig. 11c)**. The protein-ligand contacts throughout the simulation are represented in **Fig. 11d**. Water bridges, hydrogen bonds, and hydrophobic interactions were observed as the major stabilizing forces. The interactions observed during the MD simulation revealed that the

37

789 ligand binds with the protein by a polar bond at Gln127 (chain A) and positive electrostatic

790 interactions at Arg4 (chain A) and Lys5 (both chain A and B) **(Fig. 11e)**. The interaction

791 between the ligand and the protein is shown in **Fig. 11f**. The simulation trajectories showed

792 that there were stabilizing interactions such as hydrogen bonds, water bridges, and

793 hydrophobic interactions. It was clear that several residues involved in the interaction in

794 which eight residues belonged to chain A and three residues belonged to chain B. Lys5 (chain

795 B), Arg4, Lys5, and Gln127 (chain A) played a major role in the interaction with the ligand.

796 The protein and ligand conformational changes during the MD simulation studies are shown

797 in Supplementary Material **Fig. S3**. The MD simulation studies suggested that the

798 Scutifoliamide-A-replicase polyprotein 1ab complex showed stability during the simulation,

799 however, there were deviations observed during MD simulation. Further, in comparison with

800 the binding of the control and its targets, the Scutifoliamide-A-replicase polyprotein 1ab

801 complex showed better interaction. Thus, Scutifoliamide-A can be considered to be one of

802 the probable molecules against replicase polyprotein 1ab of SARS-CoV-2.

803

804

805 **Fig. 11**. The binding and stability of the docked complex of natural lead molecule
806 Scutifoliamide-A and replicase polyprotein 1ab of SARS-CoV-2 were studied by molecular
807 dynamic simulation at 100 ns. The trajectories obtained during the MD simulation is shown
808 in figure (a) Protein-ligand RMSD: Protein RMSD (Å) is shown on the y-axis, and simulation
809 time is given on the x-axis (b) Plot of the protein RMSF: RMSF (Å) is given in the y-axis and
810 atom index is showed in the x-axis (c) Plot of ligand RMSF: RMSF (Å) is shown in y-axis
811 and atom index is given in the x-axis (d) The protein-ligand contact is shown in the form of a

812 histogram. The blue, grey, pink, and green regions in the histogram represent water bridges,
813 hydrophobic interactions, ionic bonds, and hydrogen bonds respectively (e) The interactions
814 between Hyoscyamine and post-fusion conformation of the spike glycoprotein observed
815 during MD simulation (f) The protein-ligand contacts shown in the form of timeline
816 representation. The top panel shows the total number of specific contacts between receptor
817 and ligand, and the bottom panel shows the amino acid residues of the target, which is
818 interacted with the ligand.

819

820 The simulation trajectories of Tamaridone and the spike glycoprotein in its post-fusion

821 conformation are shown in **Fig. 12**. The MD simulation studies suggested that the protein

822 showed a deviation from 8.0 to 15Å in the RMSD values at 100ns **(Fig. 12a)**. This variation

823 was probably due to the interaction of Tamaridone and glycoprotein that showed

824 conformational changes. The protein RMSF deviated from 3.0 to 16.0Å **(Fig. 12b)**. The

825 ligand RMSF showed a fluctuation between 7.5 – 10.0 Å, due to the changes in the entropy

826 caused by protein-ligand interaction **(Fig. 12c)**. The protein-ligand interactions throughout

827 the simulation are shown in **Fig. 12d**. The forces that stabilized the interactions between the

828 receptor and ligand were found to be water bridges, hydrogen, and hydrophobic interactions.

829 The molecular interactions that occurred more than 10% of the MD simulation are shown in

830 **Fig. 12e**. Tamaridone interacted with the protein by hydrophobic interactions at Val1170

831 (chain A) and Tyr1187 (chain B), and polar interactions at Thr923 (chain A). The contacts

832 between the ligand and protein throughout the simulation are shown in **Fig. 12f**. The

833 trajectories of total contact such as hydrogen bonds, water bridges, and hydrophobic

834 interactions between the protein and the ligand during the simulation were evident, and

835 several residues were involved in the interaction with the ligand throughout the trajectory

836 frame. The interacting residues of chain A were identified to be Ile916, Ser919, Asp1165,

837 Val1170, and the residues that make contact with chain B were observed to be Asp932,

838 Asn935, and Tyr1187. The structural features of the protein and ligand during the MD

839 simulation are shown in Supplementary Material Fig. S4. The MD simulation studies

840 suggested that the docked complexes of Tamaridone and spike glycoprotein of SARS-CoV-2

841 showed stability throughout the simulation, and the lead molecule demonstrated better

842 binding and dynamics when compared to the binding of Chloroquine to its usual targets **(Fig.**

843 **13)**. Thus, the present study prioritized that Tamaridone can also be used as a potential lead

844 molecule towards spike glycoprotein of SARS-CoV-2.

845

846

847 **Fig. 12**. The binding and stability of the docked complex of natural lead molecule
848 Tamaridone and spike glycoprotein of SARS-CoV-2 were studied by molecular dynamic
849 simulation at 100 ns. The trajectories obtained during the MD simulation is shown in figure
850 (a) Protein-ligand RMSD: Protein RMSD (Å) is shown on the y-axis, and simulation time is
851 given on the x-axis (b) Plot of the protein RMSF: RMSF (Å) is given in the y-axis and atom
852 index is showed in the x-axis (c) Plot of ligand RMSF: RMSF (Å) is shown in y-axis and
853 atom index is given in the x-axis (d) The protein-ligand contact is shown in the form of a
854 histogram. The blue, grey, pink, and green regions in the histogram represent water bridges,
855 hydrophobic interactions, ionic bonds, and hydrogen bonds respectively (e) The interactions
856 between Hyoscyamine and post-fusion conformation of the spike glycoprotein observed
857 during MD simulation (f) The protein-ligand contacts shown in the form of timeline
858 representation. The top panel shows the total number of specific contacts between receptor
859 and ligand, and the bottom panel shows the amino acid residues of the target, which is
860 interacted with the ligand.

861

862 The trajectories of simulation studies of the docked complex of Chloroquine and glutathione-

863 S-transferase complex are shown in **Fig. 13**. The simulation results suggested that the RMSD

864 values of the protein showed a deviation from 1.6 to 3.2 Å at 100ns indicated that there were

865   fewer or no conformational changes during the simulation period **(Fig. 13a)**. The variation in

866   the RMSD of the protein was probably due to the binding with Chloroquine. The protein

867   RMSF deviated from 0.8-2.3Å **(Fig. 13b)**. Ligand RMSF deviated from 8.5-6.0Å, which

868   indicated the fluctuations corresponding to their entropy in the binding **(Fig. 13c)**. The

869   interactions that stabilized the docked complex were identified to be water bridges, ionic

870   bonds, hydrogen bonds, and hydrophobic interactions, which are shown in **Fig. 13d**. The

871   molecular interactions that occurred during >10% of the MD simulation are depicted in **Fig.**

872   **13e**. The analysis revealed that the ligand binds to the protein with hydrophobic interactions

873   with Phe94 and Tyr95 and electrostatic interaction with Lys141. The interactions between

874   ligand and the protein are depicted in **Fig. 13f**. The major forces that stabilized the binding

875   between the ligand and receptor during the simulation were identified to be hydrogen bonds,

876   ionic bonds, water bridges, and hydrophobic interactions. The number of residues involved in

877   the interaction with the ligand was less in comparison with the interaction of the selected

878   natural molecules and targets. It was observed that Phe94 showed predominant interaction

879   during the first 50ns, and Tyr95 showed maximum interaction during the next 50ns of the

880   simulation. The conformational changes of the interaction between glutathione-S-transferase

881   and chloroquine during the MD simulation are shown in Supplementary material, **Fig. S5**.

882

Fig. 13. The binding and stability of the docked complex of conventional antiviral drug Chloroquine and Glutathione-S-transferase studied by molecular dynamic simulation at 100 ns. The trajectories obtained during the MD simulation is shown in figure (a) Protein-ligand RMSD: Protein RMSD (Å) is shown on the y-axis, and simulation time is given on the x-axis (b) Plot of the protein RMSF: RMSF (Å) is given in the y-axis and atom index is showed in the x-axis (c) Plot of ligand RMSF: RMSF (Å) is shown in y-axis and atom index is given in the x-axis (d) The protein-ligand contact is shown in the form of a histogram. The blue, grey, pink, and green regions in the histogram represent water bridges, hydrophobic interactions, ionic bonds, and hydrogen bonds respectively (e) The interactions between Hyoscyamine and post-fusion conformation of the spike glycoprotein observed during MD simulation (f) The protein-ligand contacts shown in the form of timeline representation. The top panel shows the total number of specific contacts between receptor and ligand, and the bottom panel shows the amino acid residues of the target, which is interacted with the ligand.

896

3.6. Binding potential of natural lead calculated by MM-PBSA

42

898   The binding potential of the complexes of natural lead molecules and the prioritized targets

899   were confirmed by the energy calculations by MM-PBSA approaches. Gromacs force field

900   was used to calculate the binding affinities of the molecular targets and ligand complexes.

901   The interaction energy of the Chloroquine and its usual target glutathione-S-transferase was

902   estimated to be -33.12 kcal/mol. The binding energies of the docked complex of

903   Hyoscyamine and spike glycoprotein, Rotiorinol-C and replicase polyprotein 1ab,

904   Scutifoliamide-A and replicase polyprotein, and Tamaridone and spike glycoprotein were

905   estimated to be -48. 25, -38. 40, -45. 97 and -38. 79 kcal/mol, respectively. Thus, the energy

906   calculations by MMPBSA showed that the interaction of four natural lead molecules towards

907   the prioritized targets of SARS-CoV-2 demonstrated better binding interaction compared to

908   the binding of Chloroquine and Glutathione-S-transferase.

909

910   From the molecular docking, MD simulation, and energy calculation studies, it is clear that

911   the four potential natural lead molecules demonstrated better binding energies, stabilities, and

912   dynamics towards the prioritized drug targets of SARS-CoV-2 compared to the binding of

913   Chloroquine and glutathione-S-transferase. Thus, the present study revealed that natural

914   molecules and the prioritized targets can be used as potential candidates for the development

915   of therapeutic agents against COVID-19.

916

917   Recent studies emphasized that the scope of computer-aided molecular design towards the

918   lead development and identification of molecular targets of COVID-19. Studies suggested

919   that natural lead compounds screened against the targets of SARS-CoV-2 such as spike

920   glycoprotein (S), non-structural proteins (nsp), an envelope protein (E), membrane protein

921   (M) provided novel insights for drug repurposing approach against SARS-CoV-2 [78]. The

922   interaction studies between SARS-CoV spike protein and cell-surface receptor (GRP78)

923   suggested that the binding favorable occurred between the regions 480-488 of the spike

924   protein and GRP78 [79]. Mpro was identified to be a potential drug target by Jin et al (2020)

925   suggested a mechanism-based inhibitor, N3, by virtual screening [80]. Beclabuvir showed

926   significant binding towards Mpro with a binding energy of -10.4 kcal/mol and was used to

927   screen novel lead molecules by virtual screening. This drug is presently being suggested for

928   clinical trials [81]. Recent studies showed that the phytochemicals from *Psorothamnus*

929   *arborescens*, *Myrica cerifera*, and *Hyptis atrorubens* showed binding potential towards

930   Chymotrypsin like protease (CL-pro) [82]. SARS-CoV nsp6 has been shown to activate

autophagy, inducing vesicles, and is known to interact with nsp2, nsp8, nsp9, and accessory protein 9b [83]. nsp6 is considered to be one of the potential targets to suppress the virulent genes of the pathogen. Envelope (E) proteins were reported to form ion channels, which is mainly associated with pathogenesis, and the inhibition of these channels provided insights for drug discovery. A recent study suggested that Belachinal, Macaflavanone-E, and Vibsanol-B were reported to be potential inhibitors of envelope protein [84]. Similarly, another study showed that several viral peptides were modeled by computational virtual screening for vaccine development [85]. The current study predicted the binding potential of four natural lead molecules, namely Hyoscyamine, Rotiorinol-C, Scutifoliamide-A, and Tamaridone towards selected molecular targets of COVID-19, and the hypothesis probably provide profound insight for the development of therapeutic agents against putative targets of SARS-CoV-2.

The present study provides insight into the molecular mechanism of the binding potential of natural phytochemical towards fourteen molecular targets of SARS-CoV-2 for future investigation. Since there are no standard drugs available for the treatment of COVID-19 to compare our studies, the interaction models of Chloroquine and Hydroxychloroquine and their usual targets were used as the comparative control, and, therefore, this prediction could have a variation when it implements at the experimental level. Further, the study modeled the binding potential of four lead molecules towards the prioritized targets, and due to the time and resource constraints, the molecular dynamics simulation, and energy calculations were performed only for the best-docked complexes that showed minimum binding energies and maximum stabilizing interactions. The molecular dynamics and simulation studies between selected natural compounds and other targets can also be modeled to obtain significant breakthroughs for the development of potential targets and lead molecules. Thus, the present study provides an ample foundation for future investigation and developing natural lead molecules against multiple targets of SARS-CoV-2.

4. Conclusion

At present, COVID-19 is one of the most critical public health concerns with high mortality and morbidity rate worldwide. There are limited therapeutic agents available to treat the disease. Thus, there is a high emergency to identify potential therapeutic strategies to tackle COVID-19. Computer-aided virtual screening is one of the promising approaches which

44

reduce the time and cost required to develop new candidate drugs. This approach can be used to screen lead molecules with druggish and pharmacokinetic features that can be transformed into experimental levels to develop the therapeutic intervention. The natural molecules are known to have inhibitory potential towards several viral targets. The present study aimed to screen potential natural lead molecules towards multiple prospective molecular targets of SARS-CoV-2. Based on the functional and virulence role, fourteen molecular targets of SARS-CoV-2 were identified, and eleven of them were retrieved from the Protein Data Bank, and three proteins that lack the 3D structures, were computationally predicted. By an extensive literature survey and database search, ninety-two natural compounds were selected. The drug likeliness, pharmacokinetic and toxicity properties of selected lead molecules were predicted by various computational biology tools. Based on the virtual screening, four potential lead molecules were screened, and the binding potentials of these lead molecules towards fourteen targets were modeled by molecular docking. The stabilities of the four best-docked complexes were confirmed by molecular dynamic simulation and energy calculation studies. The present study suggested that the four lead molecules were qualified for the drug likeliness, pharmacokinetics, and toxicity features, and demonstrated profound binding with most of the selected targets. Notably, Hyoscyamine and Tamaridone towards spike glycoprotein and Rotiorinol-C and Scutifoliamide-A towards replicase polyprotein 1ab of SARS-CoV -2 were showed better and significant binding compared to the binding of Chloroquine and glutathione S transferase. Thus, the present study suggested that these natural lead molecules can be used as potential lead molecules against the prospective molecular targets of SARS-CoV-2, and the computational prediction probably provides a substantial breakthrough in the drug discovery pipeline to develop future therapeutic agents against COVID-19 and the prediction can be transformed into the experiential level.

Competing interest statement

The authors declare that they have no competing interests.

Funding

No funding was involved in the preparation of this manuscript or in the decision to submit it for publication.

Data availability

Data is presented within the manuscript and the supplemental materials.

Author contribution

997   Sinosh Skariyachan and Dharshini were involved in the Conceptualization; Data curation;

998   Formal analysis; Investigation; Methodology; Project administration; Resources; Software;

999   Supervision; Validation; Visualization; Roles/Writing - original draft; Writing - review &

1000 editing of the manuscript. Aditi G Muddebihalkar, Akshay Uttarkar and Vidya Niranjan

1001 involved in Investigation, Resources; Software; Supervision and Visualization; Roles/Writing

1002

1003 **References**

1004 [1]   J. F. Chan, K. H. Kok, Z. Zhu, H. Chu, K. K. To, S. Yuan, K. Y. Yuen, Genomic
1005   characterization of the 2019 novel human pathogenic coronavirus isolated from a
1006   patient with atypical pneumonia after visiting Wuhan, Emerg. Microbes. Infect. 9 (1)
1007   (2020) 221-236.

1008 [2]   World Health Organization. WHO Coronavirus Disease (COVID-19) Dashborad.
1009   December 2020. https://covid19.who.int. Retrieved 22 December 2020.

1010 [3]   S. Khan, R. Siddique, M. A. Shereen, A. Ali, J. Liu, Q. Bai, N. Bashir, M. Xue, The
1011   emergence of a novel coronavirus (SARS-CoV-2), their biology and therapeutic
1012   options, J. Clin. Microbiol. JCM.00187-20. Advance online publication. doi:
1013   10.1128/JCM.00187-20

1014 [4]   R. Verity, L. C. Okell, I. Dorigatti, P. Winskill, C. Whittaker, N. Imai, G. Cuomo-
1015   Dannenburg, H. Thompson, P. Walker, H. Fu, A. Dighe, J. T. Griffin, M. Baguelin, S.
1016   Bhatia, A. Boonyasiri, A. Cori, Z. Cucunubá, R. FitzJohn, K. Gaythorpe, W. Green, A.
1017   Hamlet, W. hinsley, D. Laydon, G. Nedjati-Gilani, S. Riley, S. van Elsland, E. Volz, H.
1018   Wang, Y. Wang, X. Xi, C. A. Donnelly, A C. Ghani, N. M. Ferguson, Estimates of the
1019   severity of coronavirus disease 2019: a model-based analysis. Lancet Infect. Dis.
1020   S1473-3099 (20) (2020) 30243-7. Advance online publication. doi: 10.1016/S1473-
1021   3099(20)30243-7

1022 [5]   F. Beerkens, M. John, B. Puliafito, V. Corbett, C. Edwards, D. Tremblay, COVID-19
1023   Pneumonia as a Cause of Acute Chest Syndrome in an Adult Sickle Cell Patient. Am. J.
1024   Hematol. Accepted Author Manuscript. (2020) doi:10.1002/ajh.25809

1025 [6]   D. Workman, D. B. Welling, B. S. Carter, W. T. Curry, E. H. Holbrook, S. T. Gray, G.
1026   A. Scangas, B. S. Bleier, Endonasal instrumentation and aerosolization risk in the era of
1027   COVID-19: simulation, literature review, and proposed mitigation strategies. Int.
1028   Forum. Allergy Rh. Accepted Author Manuscript. (2020) doi:10.1002/alr.22577

1029 [7]   W. G. Carlos, C. S. Dela Cruz, B. Cao, S. Pasnick, S. Jamil, Novel Wuhan (2019-
1030   nCoV) Coronavirus. Am. J. Respir. Crit. Care Med. 201 (4) (2020) P7–P8. doi:
1031   10.1164/rccm.2014P7

1032 [8]   Y. R. Guo, Q. D. Cao, Z. S. Hong, Y. Y. Tan, S. D. Chen, H. J. Jin, K. S. Tan, D. Y.
1033   Wang, Y. Yan, The origin, transmission and clinical therapies on coronavirus disease
1034   2019 (COVID-19) outbreak - an update on the status, Mil. Med. Res. 7 (1) (2020) 11.
1035   doi: 10.1186/s40779-020-00240-0

1036 [9]   L. E. Gralinski, V. D. Menachery, Return of the Coronavirus: 2019-nCoV, Viruses. 12
1037   (2) (2020) 135. doi: 10.3390/v12020135

1038 [10]   C. Walls, Y. Park, M. A. Tortorici, A. Wall, A. T. McGuire, D. Veesler, Structure,
1039   Function, and Antigenicity of the SARS-CoV-2 Spike Glycoprotein, Cell. (2020) doi:
1040   10.1016/j.cell.2020.02.058

1041 [11]   M. Behbahani, *In silico* Design of novel Multi-epitope recombinant vaccine based on
1042   Coronavirus surface glycoprotein, bioRxiv. (2020) doi: 10.1101/2020.03.10.985499.

1043 [12]   M. Kim, M. Cho, J. H. Lee, H. Kim, H. S. Son, Analysis of Coronaviral Spike proteins
1044   and Virus–host Interactions. KJPH. 56 (1) (2019) 25-32.

1045 [13]   Grifoni, J. Sidney, Y. Zhang, R. H. Scheuermann, B. Peters, A. Sette, A Sequence
1046   Homology and Bioinformatic Approach Can Predict Candidate Targets for Immune
1047   Responses to SARS-CoV-2, Cell Host Microbe. (2020) doi:
1048   10.1016/j.chom.2020.03.002

1049 [14]   R. Kong, G. Yang, R. Xue, M. Liu, F. Wang, J. Hu, S. Chang, COVID-19 Docking
1050   Server: An interactive server for docking small molecules, peptides and antibodies
1051   against potential targets of COVID-19. arXiv, preprint arXiv:2003.00163 (2020)

1052 [15]   M. Fahmi, Y. Kubota, M. Ito, Nonstructural proteins NS7b and NS8 are likely to be
1053   phylogenetically associated with evolution of 2019-nCoV. Infect. Genet. Evol. 81
1054   (2020) 104272. doi: 10.1016/j.meegid.2020.104272

1055 [16]   L. Zhang, D. Lin, X. Sun, U. Curth, C. Drosten, L. Sauerhering, S. Becker, K. Rox, R.
1056   Hilgenfeld, Crystal structure of SARS-CoV-2 main protease provides a basis for design
1057   of improved α-ketoamide inhibitors, Science. (2020) doi: 10.1126/science.abb3405.

1058 [17]   C. Harrison, Coronavirus puts drug repurposing on the fast track. Nat. Biotechnol.
1059   Advance online publication. (2020) doi: 10.1038/d41587-020-00003-1.

1060 [18]   Y. Zhou, Y. Hou, J. Shen, Y. Huang, W. Martin, F. Cheng, Network-based drug
1061   repurposing for novel coronavirus 2019-nCoV/SARS-CoV-2, Cell Discov. 6 (2020) 14.

1062 [19] D. H. Zhang, K. L. Wu, X. Zhang, S. Q. Deng, B. Peng, *In silico* screening of Chinese

1063   herbal medicines with the potential to directly inhibit 2019 novel coronavirus, J. Integr.

1064   Med. 18 (2) (2020) 152–158.

1065 [20] M. L. Agostini, A. J. Pruijssers, J. D. Chappell, J. Gribble, X. Lu, E. L. Andres, G. R.

1066   Bluemling, M. A. Lockwood, T. P. Sheahan, A. C. Sims, M. G. Natchus, M. Saindane,

1067   A. A. Kolykhalov, G. R. Painter, R. S. Baric, M. R. Denison, Small-Molecule Antiviral

1068   β-d-N4-Hydroxycytidine Inhibits a Proofreading-Intact Coronavirus with a High

1069   Genetic Barrier to Resistance. J. Virol. 93 (24) (2019) e01348-19.

1070 [21] H. M. Berman, J. Westbrook, Z. Feng, G. Gilliland, T. N. Bhat, H. Weissig, I. N.

1071   Shindyalov, P. E. Bourne, The Protein Data Bank. Nucleic Acids Res. 28 (2000) 235-

1072   242.

1073 [22] S. Duquerroy, A. Vigouroux, P. J. Rottier, F. A. Rey, B. J. Bosch, Central ions and

1074   lateral asparagine/glutamine zippers stabilize the post-fusion hairpin conformation of

1075   the SARS coronavirus spike glycoprotein, Virology. 335 (2) (2005) 276–285.

1076 [23] J. B. Bonanno, R. Fowler, S. Gupta, J. Hendle, D. Lorimer, R. Romero, J. M. Sauder, C.

1077   L. Wei, E. T. Liu, S. K. Burley, T. Harris, Company Says It Mapped Part of SARS

1078   Virus, New York Times 30 July. (2003) C2-C2

1079 [24] D. Fearon, C. D. Owen, A. Douangamath, P. Lukacik, A. J. Powell, C. M. Strain-

1080   Damerell, F. Resnick, T. Krojer, P. Gehrtz, C. Wild, A. Aimon, J. Brandao-Neto, A.

1081   Carbery, L. Dunnett, R. Skyner, M. Snee, N. London, M. A. Walsh, F. von Delft,

1082   PanDDA analysis group deposition of SARS-CoV-2 mainprotease fragment screen. (*To

1083   be published*).

1084 [25] J. Liu, Y. Sun, J. Qi, F. Chu, H. Wu, F. Gao, T. Li, J. Yan, G. F. Gao, The membrane

1085   protein of severe acute respiratory syndrome coronavirus acts as a dominant

1086   immunogen revealed by a clustering region of novel functionally and structurally

1087   defined cytotoxic T-lymphocyte epitopes, J. Infect. Dis. 202 (8) (2010) 1171–1180.

1088 [26] Y. Li, W. Surya, S. Claudine, J. Torres, Structure of a conserved Golgi complex-

1089   targeting signal in coronavirus envelope proteins, J. Biol. Chem. 289 (18) (2014)

1090   12535–12549.

1091 [27] C. A. Nelson, A. Pekosz, C. A. Lee, M. S. Diamond, D. H. Fremont, Structure and

1092   intracellular targeting of the SARS-coronavirus Orf7a accessory protein, Structure

1093   (London, England: 1993). 13 (1) (2005) 75–85.

1094 [28] C. Meier, A. R. Aricescu, R. Assenberg, R. T. Aplin, R. J. Gilbert, J. M. Grimes, D. I.
1095   Stuart, The crystal structure of ORF-9b, a lipid binding protein from the SARS
1096   coronavirus, Structure (London, England: 1993). 14 (7) (2006) 1157–1165.

1097 [29] R. Yan, Y. Zhang, Y. Li, L. Xia, Y. Guo, Q. Zhou, Structural basis for the recognition
1098   of SARS-CoV-2 by full-length human ACE2, Science (New York, N.Y.) 367 (6485)
1099   (2020) 1444–1448. doi:10.1126/science.abb2762

1100 [30] Y. Gao, L. Yan, Y. Huang, F. Liu, Y. Zao, L. Cao, T. Wang, Q. Sun, Z. Ming, L.
1101   Zhang, J. Ge, L. Zheng, Y. Zhang, H. Wang, Y. Zhu, C. Zhu, T. Hu, T. Hua, T. Hua, B.
1102   Zhang, X. Yang, J. Li, H. Yang, Z. Liu, W. Xu, L. W. Guddat, Q. Wang, Z. Luo, Z.
1103   Rao, Structure of the RNA-dependent RNA polymerase from COVID-19 virus,
1104   Science. (2020).

1105 [31] UniProt, Consortium. UniProt: A hub for protein information. Nucleic Acids Res. 43
1106   (Database issue) (2015) D204–12.

1107 [32] C. Zhang, W. Zheng, X. Huang, E. W. Bell, X. Zhou, Y. Zhang, Protein structure and
1108   sequence re-analysis of 2019-nCoV genome refutes snakes as its intermediate host and
1109   the unique similarity between its spike protein insertions and HIV-1, J. Proteome Res.
1110   (2020) doi: 10.1021/acs.jproteome.0c00129

1111 [33] D. Xu, Y. Zhang, Improving the physical realism and structural accuracy of protein
1112   models by a two-step atomic-level energy minimization, Biophys. J. 101 (10) (2011)
1113   2525–2534. doi: 10.1016/j.bpj.2011.10.024

1114 [34] M. Heinig, D. Frishman, STRIDE: a web server for secondary structure assignment
1115   from known atomic coordinates of proteins, Nucleic Acids Res. 32 (Web Server issue)
1116   (2004) W500–W502.

1117 [35] J. Wiederstein, M. Sippl, ProSA-web: Interactive web service for the recognition of
1118   errors in three-dimensional structures of proteins, Nucleic Acids Res. 35 (Web Server)
1119   (2007) W407–W410. doi:10.1093/nar/gkm290

1120 [36] R. Luthy, J. U. Bowie, D. Eisenberg, Assessment of protein models with three-
1121   dimensional profiles, Nature. 356 (1992) 83–85. doi:10.1038/356083a0

1122 [37] Laskowski, W. MacArthur, D. Moss, M. Thornton, PROCHECK: A program to check
1123   the stereochemical quality of protein structures. J. Appl. Crystallogr. 26 (2) (1993) 283–
1124   291. doi:10.1107/S0021889892009944

1125 [38] Colovos, T. Yeates, Verification of protein structures: Patterns of non-bonded atomic
1126   interactions, Protein Sci. 2 (9) (1993) 1511–1519. doi:10.1002/pro.5560020916

1127 [39] S. Torsten, K. Jurgen, G. Nicolas, P. Manuel, SWISS-MODEL: An automated protein
1128   homology-modeling server, Nucleic Acids Res. 31 (2003) 3381–3385.

1129 [40] S. Kim, J. Chen, T. Cheng, A. Gindulyte, J. He, S. He, Q. Li, B. A. Shoemaker, P. A.
1130   Thiessen, B. Yu, L. Zaslavsky, J. Zhang, E. E. Bolton, PubChem 2019 update:
1131   improved access to chemical data, Nucleic Acids Res. 47 (D1) (2019) D1102-1109.

1132 [41] H. E. Pence, A. Williams, ChemSpider: An online chemical information resource, J.
1133   Chem. Educ. 87(11) (2010) 1123–1124. doi:10.1021/ed100697w

1134 [42] N. M. O'Boyle, M. Banck, C. A. James, C. Morley, T. Vandermeersch, G. R.
1135   Hutchison, Open Babel: An open chemical toolbox. J. Cheminformatics. 3 (1) (2011)
1136   33.

1137 [43] F. Veber, R. Johnson, H. Y. Chen, B. R. Smith, K. W. Ward, K. D. Kopple, Molecular
1138   properties that influence the oral bioavailability of drug candidates, J. Med. Chem. 45
1139   (2002) 2615–2623.

1140 [44] Daina, O. Michielin, V. Zoete, SwissADME: a free web tool to evaluate
1141   pharmacokinetics, drug-likeness and medicinal chemistry friendliness of small
1142   molecules, Sci. Rep. 7 (2017) 42717.

1143 [45] Lipinski, F. Lombardo, B. Dominy, P. Feeney, Experimental and computational
1144   approaches to estimate solubility and permeability in drug discovery and development
1145   settings. Adv. Drug Deliv. Rev. 46 (2001) 3–26.

1146 [46] W. J. Egan, W. P. Walters, M. A. Murcko, Guiding molecules towards drug-likeness,
1147   Curr. Opin Drug Disc. Devel. 5 (4) (2002) 540–549.

1148 [47] T. Frimurer, R. Bywater, L. Nærum, L. Lauritsen, S. Brunak, Improving the odds in
1149   discriminating "drug-like" from "nondrug-like" compounds. J. Chem. Inf. Comput. Sci.
1150   40 (2000) 1315–1324.

1151 [48] K. Ghose, V. N. Viswanadhan, J. J. Wendoloski, A knowledge-based approach in
1152   designing combinatorial or medicinal chemistry libraries for drug discovery. 1. A
1153   qualitative and quantitative characterization of known drug databases, J. Comb. Chem.
1154   1 (1) (1999) 55–68.

1155 [49] Ajay, P. Walters, A. Murcko, Can we learn to distinguish between "drug-like" and
1156   "nondrug-like" molecules?, J. Med. Chem. 41 (1998) 3314–332.

1157 [50] Y. C. Martin, A bioavailability score. J. Med. Chem. 48 (9) (2005) 3164–3170.

1158 [51] Ajay, W. Bemis, A. Murcko, Blood brain barrier: design in libraries with CNS activity.
1159   J.Med. Chem. 42 (1999) 4942–4951.

1160 [52] M. Yazdanian, L. Glynn, L. Wright, Hawi, Correlating partitioning and Caco-2 cell
1161   permeability of structurally diverse small molecular weight compounds. Pharm. Res. 15
1162   (1998) 1490–1494.

1163 [53] D. Irvine, L. Takahashi, K. Lockhart, J. Cheong, W. Tolan, E. Selick, R. Grove, MDCK
1164   (Madin-Darby canine kidney) cells: a tool for membrane permeability screening. J.
1165   Pharm. Sci. 88 (1999) 28–33.

1166 [54] Daina, O. Michielin, V. Zoete, iLOGP: A Simple, Robust, and Efficient Description of
1167   n-Octanol/Water Partition Coefficient for Drug Design Using the GB/SA Approach. J.
1168   Chem. Inf. Model. 54 (12) (2014) 3284-3301.

1169 [55] J. S. Delaney, ESOL: estimating aqueous solubility directly from molecular structure. J.
1170   Chem Inf. Comput. Sci. 44 (3) (2004) 1000–1005.

1171 [56] K. Mortelmans, E. Zeiger, The Ames Salmonella/microsome mutagenicity assay.
1172   Mutat. Res. 2 (2020) 29–60.

1173 [57] O. Trott, A. J. Olson, AutoDock Vina: Improving the speed and accuracy of docking
1174   with a new scoring function, efficient optimization and multithreading. J. Comput.
1175   Chem. 31 (2010) 455–461.

1176 [58] K. P. Tan, R. Varadarajan, M. S. Madhusudhan, DEPTH: a web server to compute
1177   depth and predict small-molecule binding cavities in proteins, Nucleic Acids Res. 39 (2)
1178   (2011) W242–W248.

1179 [59] W. Tian, C. Chen, X. Lei, J. Zhao, J. Liang, CASTp 3.0: computed atlas of surface
1180   topography of proteins, Nucleic Acids Res. 46 (W1) (2018) W363–W367.

1181 [60] Schrödinger Release 2019-3: Desmond Molecular Dynamics System, D. E. Shaw
1182   Research, New York, NY, 2019. Maestro-Desmond Interoperability Tools,
1183   Schrödinger, New York, NY, 2019

1184 [61] N. A. Baker, D. Sept, S. Joseph, M. J. Holst, J. A. McCammon, Electrostatics of
1185   nanosystems: application to microtubules and the ribosome, PNAS U.S.A. 98 (18)
1186   (2001) 10037–10041.

1187 [62] R. Kumari, R. Kumar, Open Source Drug Discovery Consortium, A. Lynn, g_mmpbsa-
1188   -a GROMACS tool for high-throughput MM-PBSA calculations. J. Chem. Inf. Model.
1189   54 (7) (2014) 1951–1962.

1190 [63] S. Pronk, S. Páll, R. Schulz, P. Larsson, P. Bjelkmar, R. Apostolov, M. R. Shirts, J. C.
1191   Smith, P. M. Kasson, D. van der Spoel, B. Hess, E. Lindahl, GROMACS 4.5: a high-

1192   throughput and highly parallel open source molecular simulation toolkit,
1193   Bioinformatics. 29 (7) (2013) 845–854.

1194 [64] S. K. Wong, W. Li, M. J. Moore, H. Choe, M. Farzan, A 193-amino acid fragment of
1195   the SARS coronavirus S protein efficiently binds angiotensin-converting enzyme 2, J.
1196   Biol. Chem. 279 (2004) 3197-3201.

1197 [65] S. A. Jeffers, S. M. Tusell, L. Gillim-Ross, E. M. Hemmila, J. E. Achenbach, G. J.
1198   Babcock, W. D. Thomas Jr, L. B. Thackray, M. D. Young, R. J. Mason, D. M.
1199   Ambrosino, D. E. Wentworth, J. C. Demartini, K. V. Holmes, CD209L (L-SIGN) is a
1200   receptor for severe acute respiratory syndrome coronavirus, PNAS. U.S.A. 101 (2004)
1201   15748-15753.

1202 [66] K. G. Lokugamage, K. Narayanan, C. Huang, S. Makino, Severe acute respiratory
1203   syndrome coronavirus protein nsp1 is a novel eukaryotic translation inhibitor that
1204   represses multiple steps of translation initiation, J. Virol. 86 (2012) 13598-13608.

1205 [67] J. L. Nieto-Torres, C. Verdia-Baguena, J. M. Jimenez-Guardeno, J. A. Regla-Nava, C.
1206   Castano-Rodriguez, R. Fernandez-Delgado, J. Torres, V. M. Aguilella, L. Enjuanes,
1207   Severe acute respiratory syndrome coronavirus E protein transports calcium ions and
1208   activates the NLRP3 inflammasome, Virology. 485 (2015) 330-339.

1209 [68] Huang, K. G. Lokugamage, J. M. Rozovics, K. Narayanan, B. L. Semler, S. Makino,
1210   SARS coronavirus nsp1 protein induces template-dependent endonucleolytic cleavage
1211   of mRNAs: viral mRNAs are resistant to nsp1-induced RNA cleavage, PLoS Pathog. 7
1212   (2011) E1002433-E1002433.

1213 [69] Y. J. Tan, P. Y. Tham, D. Z. Chan, C-F. Chou, S. Shen, B. C. Fielding, T. H. Tan, S. G.
1214   Lim, W. Hong, The severe acute respiratory syndrome coronavirus 3a protein up-
1215   regulates expression of fibrinogen in lung epithelial cells, J. Virol. 79 (2005) 10083-
1216   10087.

1217 [70] Y. J. Tan, B. C. Fielding, P. Y. Goh, S. Shen, T. H. P. Tan, S. G. Lim, W. Hong,
1218   Overexpression of 7a, a protein specifically encoded by the severe acute respiratory
1219   syndrome coronavirus, induces apoptosis via a caspase-dependent pathway, J. Virol. 78
1220   (2004) 14043-14047.

1221 [71] E. M. Cottam, M. C. Whelband, T. Wileman, Coronavirus NSP6 restricts
1222   autophagosome expansion, Autophagy. 10 (2014)1426-1441.

1223 [72] J. te Velthuis, S. H. van den Worm, E. J. Snijder, The SARS-coronavirus nsp7+nsp8
1224   complex is a unique multimeric RNA polymerase capable of both de novo initiation and
1225   primer extension, Nucleic Acids Res. 40 (2012)1737-1747.

1226 [73] M. Bouvet, I Imbert, L. Subissi, L. Gluais, B. Canard, E. Decroly, RNA 3'-end
1227   mismatch excision by the severe acute respiratory syndrome coronavirus nonstructural
1228   protein nsp10/nsp14 exoribonuclease complex, PNAS. U.S.A. 109 (2012) 9372-9377.

1229 [74] S. A. Helgeson, E. J. Mwakyanjala, P. P. Parikh, K. L. Venkatachalam, Hyoscyamine
1230   for a Slow Ventricular Response During Atrial Fibrillation, Ann. Intern. Med. 169 (6)
1231   (2018) 418–419. doi: 10.7326/L18-0037

1232 [75] N. Gupta, Hyoscyamine for a Slow Ventricular Response During Atrial Fibrillation,
1233   Ann. Intern. Med. 70 (10) (2019) 735. doi: 10.7326/L19-0092

1234 [76] S. Kanokmedhakul, K. Kanokmedhakul, P. Nasomjai, S. Louangsysouphanh, K.
1235   Soytong, M. Isobe, P. Kongsaeree, S. Prabpai, A. Suksamrarn, Antifungal azaphilones
1236   from the fungus Chaetomium cupreum CC3003, J. Nat. Prod. 69 (6) (2006) 891–895.
1237   doi: 10.1021/np060051v

1238 [77] J. V. Marques, R. O. Kitamura, J. H. Lago, M. C. Young, E. F. Guimarães, M. J. Kato,
1239   Antifungal amides from *Piper scutifolium* and *Piper hoffmanseggianum*, J. Nat. Prod.
1240   70 (12) (2007) 2036–2039. oid:10.1021/np070347g

1241 [78] Wu, Y. Liu, Y. Yang, P. Zhang, W. Zhong, Y. Wang, Q. Wang, Y. Xu, M. Li, X. Li, M.
1242   Zheng, L. Chen, H. Li, Analysis of therapeutic targets for SARS-CoV-2 and discovery
1243   of potential drugs by computational methods, Acta Pharm. Sin. B. (2020). doi:
1244   10.1016/j.apsb.2020.02.008

1245 [79] M. Ibrahim, D. H. Abdelmalek, M. E. Elshahat, A. A. Elfiky, COVID-19 spike-host cell
1246   receptor   GRP78   binding   site   prediction,   J.   Infection.   (2020).
1247   doi:10.1016/j.jinf.2020.02.026

1248 [80] Z. Jin, X. Du, Y. Xy, Y. Deng, M. Liu, Y. Zhao, B. Zhang, X. Li, L. Zhang, Y. Duan, J.
1249   Yu, L. Wang, K. Yang, F. Liu, T. You, X. Liu, X. Yang, F. Bai, H. Liu, X. Liu, L. W.
1250   Guddat, G. Xiao, C. Qi, Z. Shi, H. Jiang, Z. Rao, H. Yang, Structure-based drug design,
1251   virtual screening and high-throughput screening rapidly identify antiviral leads targeting
1252   COVID-19, bioRxiv. (2020). doi: 10.1101/2020.02.26.964882

1253 [81] S. Talluri, Virtual Screening Based Prediction of Potential Drugs for COVID-19,
1254   Preprints 2020, 2020020418. (2020). doi: 10.20944/preprints202002.0418.v2

1255 [82] M. T. ul Qamar, S. M. Alqahtani, M. A. Alamri, L. Chen, Structural basis of SARS-
1256   CoV-2 3CLpro and anti-COVID-19 drug discovery from medicinal plants, J. Pharm.
1257   Anal. (2020). doi: 10.1016/j.jpha.2020.03.009

1258 [83] B. W. Neuman, Bioinformatics and functional analyses of coronavirus non-structural
1259   proteins involved in the formation of replicative organelles, Antiviral Res.135 (2016)
1260   97-107. doi: 10.1016/j.antiviral.2016.10.005

1261 [84] M. K. Gupta, S. Vemula, R. Donde, G. Gouda, L. Behera, R. Vadde, In-silico
1262   approaches to detect inhibitors of the human severe acute respiratory syndrome
1263   coronavirus envelope protein ion channel, J. Biomol. Struct. Dyn. (2020) 1–11.
1264   Advance online publication. doi: 10.1080/07391102.2020.1751300

1265 [85] Hyun-Jung Lee, H. Koohy, *In silico* identification of vaccine targets for 2019-nCoV.
1266   F1000Research. 9 (2020) 145. doi: 10.12688/f1000research.22507.1

1267

1268

1269

Figure legends

Fig.1. Computational modeling and model validation of Protein3a (a) Theoretical model of the target protein modeled using C-I-Tasser, (b) Secondary structure prediction of the theoretical model by STRIDE (c) Ramachandran plot assessment of the modeled residues of the target protein obtained by ProCheck (d) Stereo-chemical validation of the theoretical model in terms of z-score obtained from ProSA (e) The residues qualifying the 3D-1D score predicted by Verify 3D (f) The quality factor of the model obtained by the output plot of error function predicted by ERRAT.

Fig.2. Computational modeling and model validation of Protein6 (a) Theoretical model of the target protein modeled using C-I-Tasser, (b) Secondary structure prediction of the theoretical model by STRIDE (c) Ramachandran plot assessment of the modeled residues of the target protein obtained by ProCheck (d) Stereo-chemical validation of the theoretical model in terms of z-score obtained from ProSA (e) The residues qualifying the 3D-1D score predicted by Verify 3D (f) The quality factor of the model obtained by the output plot of error function predicted by ERRAT.

Fig.3. Computational modeling and model validation of Protein10 (a) Theoretical model of the target protein modeled using C-I-Tasser, (b) Secondary structure prediction of the theoretical model by STRIDE (c) Ramachandran plot assessment of the modeled residues of the target protein obtained by ProCheck (d) Stereo-chemical validation of the theoretical model in terms of z-score obtained from ProSA (e) The residues qualifying the 3D-1D score predicted by Verify 3D (f) The quality factor of the model obtained by the output plot of error function predicted by ERRAT

Fig. 4. Prediction of the binding potential of Hyoscyamine towards the prioritized molecular targets of SARS-CoV by molecular docking visualized in MGL tools of AutoDock. The figure displayed the binding pocket of the ligand-receptor complex. The interacting residues and the ligands are displayed in stick figures. The interacting residues and binding energy are labeled (a) Binding of the ligand and post-fusion conformation of spike glycoprotein (binding energy: -8.14 kcal/mol) (b) Binding of the ligand and open state spike glycoprotein (binding energy: -6.0 kcal/mol) (c) Binding of the ligand and closed state spike glycoprotein (binding energy -5.7 kcal/mol) (d) Binding of the ligand and replicase polyprotein 1ab (binding

energy: -6.1 kcal/mol) (e) Binding of the ligand and receptor binding domain of membrane protein (binding energy: -5.4 kcal/mol) (f) Binding of the ligand and membrane protein (binding energy: -0.7 kcal/mol) (g) Binding of the ligand and small envelope protein (binding energy: -2.2 kcal/mol) (h) Binding of the ligand and replicase polyprotein 1a (binding energy: -6.0 kcal/mol) (i) Binding of the ligand and protein3a (binding energy: -6.1 kcal/mol) (j) Binding of the ligand and protein7a (binding energy: -4.4 kcal/mol) (k) Binding of the ligand and protein 9b (binding energy: -4.4 kcal/mol) (l) Binding of the ligand and non-structural protein7 (binding energy: -5.3 kcal/mol) (m) Binding of the ligand and non-structural protein 8 (binding energy: -5.9 kcal/mol) (n) Binding of the ligand and non-structural protein12 (binding energy: -5.4 kcal/mol) (o) Binding of the ligand and non-structural protein 6 (binding energy: -5.2 kcal/mol) (p) Binding of the ligand and non-structural protein 10 (binding energy: -6.1 kcal/mol)

Fig. 5. Prediction of the binding potential of Rotiorinol-C towards the prioritized molecular targets of SARS-CoV by molecular docking visualized in MGL tools of AutoDock. The figure displayed the binding pocket of the ligand-receptor complex. The interacting residues and the ligands are displayed in stick figures. The interacting residues and binding energy are labeled (a) Binding of the ligand and post-fusion conformation of spike glycoprotein (binding energy: -6.5 kcal/mol) (b) Binding of the ligand and open state spike glycoprotein (binding energy: -6.3 kcal/mol) (c) Binding of the ligand and closed state spike glycoprotein (binding energy -6.2 kcal/mol) (d) Binding of the ligand and replicase polyprotein 1ab (binding energy: -9.8 kcal/mol) (e) Binding of the ligand and receptor binding domain of membrane protein (binding energy: -6.1 kcal/mol) (f) Binding of the ligand and membrane protein (binding energy: -0.6 kcal/mol) (g) Binding of the ligand and small envelope protein (binding energy: -2.2 kcal/mol) (h) Binding of the ligand and replicase polyprotein 1a (binding energy: -6.7 kcal/mol) (i) Binding of the ligand and protein3a (binding energy: -6.3 kcal/mol) (j) Binding of the ligand and protein7a (binding energy: -5.4 kcal/mol) (k) Binding of the ligand and protein 9b (binding energy: -5.0 kcal/mol) (l) Binding of the ligand and non-structural protein7 (binding energy: -5.3 kcal/mol) (m) Binding of the ligand and non-structural protein 8 (binding energy: -5.9 kcal/mol) (n) Binding of the ligand and non-structural protein12 (binding energy: -6.6 kcal/mol) (o) Binding of the ligand and non-structural protein 6 (binding energy: -5.6 kcal/mol) (p) Binding of the ligand and non-structural protein 10 (binding energy: -6.8 kcal/mol)

56

Fig. 6. Prediction of the binding potential of Scutifoliamide-A towards the prioritized molecular targets of SARS-CoV by molecular docking visualized in MGL tools of AutoDock. The figure displayed the binding pocket of the ligand-receptor complex. The interacting residues and the ligands are displayed in stick figures. The interacting residues and binding energy are labeled (a) Binding of the ligand and post-fusion conformation of spike glycoprotein (binding energy: -6.4 kcal/mol) (b) Binding of the ligand and open state spike glycoprotein (binding energy: -6.6 kcal/mol) (c) Binding of the ligand and closed state spike glycoprotein (binding energy -5.4 kcal/mol) (d) Binding of the ligand and replicase polyprotein 1ab (binding energy: -6.9 kcal/mol) (e) Binding of the ligand and receptor binding domain of membrane protein (binding energy: -5.9 kcal/mol) (f) Binding of the ligand and membrane protein (binding energy: -0.7 kcal/mol) (g) Binding of the ligand and small envelope protein (binding energy: -0.8 kcal/mol) (h) Binding of the ligand and replicase polyprotein 1a (binding energy: -6.8 kcal/mol) (i) Binding of the ligand and protein3a (binding energy: -5.4 kcal/mol) (j) Binding of the ligand and protein7a (binding energy: -5.6 kcal/mol) (k) Binding of the ligand and protein 9b (binding energy: -4.4 kcal/mol) (l) Binding of the ligand and non-structural protein7 (binding energy: -5.9 kcal/mol) (m) Binding of the ligand and non-structural protein 8 (binding energy: -6.0 kcal/mol) (n) Binding of the ligand and non-structural protein12 (binding energy: -6.1 kcal/mol) (o) Binding of the ligand and non-structural protein 6 (binding energy: -5.5 kcal/mol) (p) Binding of the ligand and non-structural protein 10 (binding energy: -5.6 kcal/mol)

Fig. 7. Prediction of the binding potential of Tamaridone towards the prioritized molecular targets of SARS-CoV by molecular docking visualized in MGL tools of AutoDock. The figure displayed the binding pocket of the ligand-receptor complex. The interacting residues and the ligands are displayed in stick figures. The interacting residues and binding energy are labeled (a) Binding of the ligand and post-fusion conformation of spike glycoprotein (binding energy: -7.2 kcal/mol) (b) Binding of the ligand and open state spike glycoprotein (binding energy: -7.3 kcal/mol) (c) Binding of the ligand and closed state spike glycoprotein (binding energy -6.8 kcal/mol) (d) Binding of the ligand and replicase polyprotein 1ab (binding energy: -6.3 kcal/mol) (e) Binding of the ligand and receptor-binding domain of membrane protein (binding energy: -6.5 kcal/mol) (f) Binding of the ligand and membrane protein (binding energy: -0.8 kcal/mol) (g) Binding of the ligand and small envelope protein (binding energy: -3.1 kcal/mol) (h) Binding of the ligand and replicase polyprotein 1a (binding energy:

-7.0 kcal/mol) (i) Binding of the ligand and protein3a (binding energy: -6.6 kcal/mol) (j) Binding of the ligand and protein7a (binding energy: -5.7 kcal/mol) (k) Binding of the ligand and protein 9b (binding energy: -5.6 kcal/mol) (l) Binding of the ligand and non-structural protein7 (binding energy: -5.9 kcal/mol) (m) Binding of the ligand and non-structural protein 8 (binding energy: -6.0 kcal/mol) (n) Binding of the ligand and non-structural protein12 (binding energy: -6.7 kcal/mol) (o) Binding of the ligand and non-structural protein 6 (binding energy: -5.6 kcal/mol) (p) Binding of the ligand and non-structural protein 10 (binding energy: -6.7 kcal/mol

Fig. 8. Prediction of the binding of conventional antiviral drugs towards their usual drug targets by molecular docking studies (a) Interaction of Chloroquine with its usual targets glutathione S transferase of Plasmodium falciparum (b) Binding affinity of Chloroquine towards glutathione S transferase (binding energy: -3.7 kcal/mol) illustrated the major residues involved in the interaction with the ligand (c) Interaction of Hydroxy-chloroquine with usual target human angiotensin-converting enzyme 2 (hACE2) (d) Binding affinity of Hydroxyl-chloroquine towards hACE2 (binding energy:-1.0 kcal/mol) illustrated the major residues involved in the interaction with the ligand.

Fig. 9. The binding and stability of the docked complex of natural lead molecule Hyoscyamine and spike glycoprotein of SARS-CoV-2 were studied by molecular dynamic simulation at 100 ns. The trajectories obtained during the MD simulation is shown in figure (a) Protein-ligand RMSD: Protein RMSD (Å) is shown on the y-axis, and simulation time is given on the x-axis (b) Plot of the protein RMSF: RMSF (Å) is given in the y-axis and atom index is showed in the x-axis (c) Plot of ligand RMSF: RMSF (Å) is shown in y-axis and atom index is given in the x-axis (d) The protein-ligand contact is shown in the form of a histogram. The blue, grey, pink, and green regions in the histogram represent water bridges, hydrophobic interactions, ionic bonds, and hydrogen bonds respectively (e) The interactions between Hyoscyamine and post-fusion conformation of the spike glycoprotein observed during MD simulation (f) The protein-ligand contacts shown in the form of timeline representation. The top panel shows the total number of specific contacts between receptor and ligand, and the bottom panel shows the amino acid residues of the target, which is interacted with the ligand.

Fig. 10. The binding and stability of the docked complex of natural lead molecule Rotiorinol-C and replicase polyprotein 1ab of SARS-CoV-2 studied by molecular dynamic simulation at 100 ns. The trajectories obtained during the MD simulation is shown in figure (a) Protein-ligand RMSD: Protein RMSD (Å) is shown on the y-axis, and simulation time is given on the x-axis (b) Plot of the protein RMSF: RMSF (Å) is given in the y-axis and atom index is showed in the x-axis (c) Plot of ligand RMSF: RMSF (Å) is shown in y-axis and atom index is given in the x-axis (d) The protein-ligand contact is shown in the form of a histogram. The blue, grey, pink, and green regions in the histogram represent water bridges, hydrophobic interactions, ionic bonds, and hydrogen bonds respectively (e) The interactions between Hyoscyamine and post-fusion conformation of the spike glycoprotein observed during MD simulation (f) The protein-ligand contacts shown in the form of timeline representation. The top panel shows the total number of specific contacts between receptor and ligand, and the bottom panel shows the amino acid residues of the target, which is interacted with the ligand.

Fig. 11. The binding and stability of the docked complex of natural lead molecule Scutifoliamide-A and replicase polyprotein 1ab of SARS-CoV-2 were studied by molecular dynamic simulation at 100 ns. The trajectories obtained during the MD simulation is shown in figure (a) Protein-ligand RMSD: Protein RMSD (Å) is shown on the y-axis, and simulation time is given on the x-axis (b) Plot of the protein RMSF: RMSF (Å) is given in the y-axis and atom index is showed in the x-axis (c) Plot of ligand RMSF: RMSF (Å) is shown in y-axis and atom index is given in the x-axis (d) The protein-ligand contact is shown in the form of a histogram. The blue, grey, pink, and green regions in the histogram represent water bridges, hydrophobic interactions, ionic bonds, and hydrogen bonds respectively (e) The interactions between Hyoscyamine and post-fusion conformation of the spike glycoprotein observed during MD simulation (f) The protein-ligand contacts shown in the form of timeline representation. The top panel shows the total number of specific contacts between receptor and ligand, and the bottom panel shows the amino acid residues of the target, which is interacted with the ligand.

Fig. 12. The binding and stability of the docked complex of natural lead molecule Tamaridone and spike glycoprotein of SARS-CoV-2 were studied by molecular dynamic simulation at 100 ns. The trajectories obtained during the MD simulation is shown in figure (a) Protein-ligand RMSD: Protein RMSD (Å) is shown on the y-axis, and simulation time is

given on the x-axis (b) Plot of the protein RMSF: RMSF (Å) is given in the y-axis and atom index is showed in the x-axis (c) Plot of ligand RMSF: RMSF (Å) is shown in y-axis and atom index is given in the x-axis (d) The protein-ligand contact is shown in the form of a histogram. The blue, grey, pink, and green regions in the histogram represent water bridges, hydrophobic interactions, ionic bonds, and hydrogen bonds respectively (e) The interactions between Hyoscyamine and post-fusion conformation of the spike glycoprotein observed during MD simulation (f) The protein-ligand contacts shown in the form of timeline representation. The top panel shows the total number of specific contacts between receptor and ligand, and the bottom panel shows the amino acid residues of the target, which is interacted with the ligand.

Fig. 13. The binding and stability of the docked complex of conventional antiviral drug Chloroquine and Glutathione-S-transferase studied by molecular dynamic simulation at 100 ns. The trajectories obtained during the MD simulation is shown in figure (a) Protein-ligand RMSD: Protein RMSD (Å) is shown on the y-axis, and simulation time is given on the x-axis (b) Plot of the protein RMSF: RMSF (Å) is given in the y-axis and atom index is showed in the x-axis (c) Plot of ligand RMSF: RMSF (Å) is shown in y-axis and atom index is given in the x-axis (d) The protein-ligand contact is shown in the form of a histogram. The blue, grey, pink, and green regions in the histogram represent water bridges, hydrophobic interactions, ionic bonds, and hydrogen bonds respectively (e) The interactions between Hyoscyamine and post-fusion conformation of the spike glycoprotein observed during MD simulation (f) The protein-ligand contacts shown in the form of timeline representation. The top panel shows the total number of specific contacts between receptor and ligand, and the bottom panel shows the amino acid residues of the target, which is interacted with the ligand.
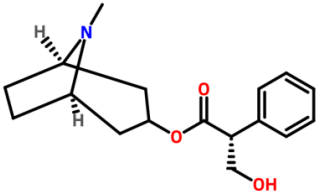
60

1460 **Table legends**

1461 **Table 1**. The structural description of eleven probable drug targets (with known 3D

1462 structures) that are involved in the virulence and pathogenesis of SARS-CoV-2

1463

1464 **Table 2**. The computational validation description of 3 probable drug targets of SARS-CoV-

1465 2 causing COVID-19 that are involved in the pathogenesis mechanism of coronavirus

1466 modeled by ab initio approach using the C-I tasser server.

1467

1468 **Table 3**. The binding potential of selected natural lead molecules towards the probable drug

1469 targets of human SARS-CoV-2 predicted by molecular docking studies by AutoDock and

1470 AutoDock Vina

1471

1472 **Supplementary materials**

1473 **Supplementary figures**

1474 **Fig. S1**. The MD simulation analysis of the post-fusion conformation of the spike
1475 glycoprotein (a) The secondary structural conformation of the proteins specifying the amino
1476 acid residues observed during the MD simulation (b) The conformational changes of
1477 secondary structural elements (SSE) of each of the residues overtime during MD simulation
1478 (c) The stability of SSE observed throughout the simulation at 100 ns. (d) MD simulation
1479 analysis of the ligand Hyoscyamine. The 2D representation of the ligand (e) The 2D
1480 representation with the color-coded rotatable bonds (f) The major ligand features observed
1481 during the MD simulation of 100 ns such as ligand RMSD, the radius of gyration (rGyr),
1482 intramolecular hydrogen bonds (intraHB), molecular surface area (MolSA), solvent
1483 accessible surface area (SASA) and polar surface area (PSA) monitored throughout the
1484 simulation (g) The torsion profiles (dial plot and bar plot) of the ligand for the rotatable bond
1485 is shown in various colors.

1486

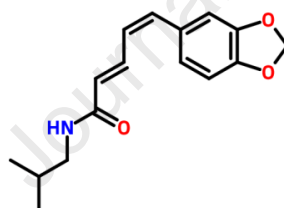1487 **Fig. S2**. The MD simulation analysis of Replicase polyprotein 1ab (a) The secondary
1488 structural conformation of the proteins specifying the amino acid residues observed during
1489 the MD simulation (b) The conformational changes of secondary structural elements (SSE) of
1490 each of the residues overtime during MD simulation (c) The stability of SSE observed
1491 throughout the simulation at 100 ns. (d) MD simulation analysis of the ligand Rotiorinol-C.
1492 The 2D representation of the ligand (e) The 2D representation with the color-coded rotatable
1493 bonds (f) The major ligand features observed during the MD simulation of 100 ns such as
1494 ligand RMSD, the radius of gyration (rGyr), intramolecular hydrogen bonds (intraHB),
1495 molecular surface area (MolSA), solvent accessible surface area (SASA) and polar surface
1496 area (PSA) monitored throughout the simulation (g) The torsion profiles (dial plot and bar
1497 plot) of the ligand for the rotatable bond is shown in various colors.

1498

1499 **Fig. S3**. The MD simulation analysis of the post-fusion conformation of the spike
1500 glycoprotein (a) The secondary structural conformation of the proteins specifying the amino
1501 acid residues observed during the MD simulation (b) The conformational changes of
1502 secondary structural elements (SSE) of each of the residues overtime during MD simulation
1503 (c) The stability of SSE observed throughout the simulation at 100 ns. (d) MD simulation
1504 analysis of the ligand Scutifoliamide-A. The 2D representation of the ligand (e) The 2D

representation with the color-coded rotatable bonds (f) The major ligand features observed during the MD simulation of 100 ns such as ligand RMSD, the radius of gyration (rGyr), intramolecular hydrogen bonds (intraHB), molecular surface area (MolSA), solvent accessible surface area (SASA) and polar surface area (PSA) monitored throughout the simulation (g) The torsion profiles (dial plot and bar plot) of the ligand for the rotatable bond is shown in various colors.

Fig. S4. The MD simulation analysis of the spike glycoprotein (a) The secondary structural conformation of the proteins specifying the amino acid residues observed during the MD simulation (b) The conformational changes of secondary structural elements (SSE) of each of the residues overtime during MD simulation (c) The stability of SSE observed throughout the simulation at 100 ns. (d) MD simulation analysis of the ligand Tamaridone. The 2D representation of the ligand (e) The 2D representation with the color-coded rotatable bonds (f) The major ligand features observed during the MD simulation of 100 ns such as ligand RMSD, the radius of gyration (rGyr), intramolecular hydrogen bonds (intraHB), molecular surface area (MolSA), solvent accessible surface area (SASA) and polar surface area (PSA) monitored throughout the simulation (g) The torsion profiles (dial plot and bar plot) of the ligand for the rotatable bond is shown in various colors.

Fig. S5. The MD simulation analysis of glutathione-S-transferase (a) The secondary structural conformation of the proteins specifying the amino acid residues observed during the MD simulation (b) The conformational changes of secondary structural elements (SSE) of each of the residues overtime during MD simulation (c) The stability of SSE observed throughout the simulation at 100 ns. (d) MD simulation analysis of the antiviral drug Chloroquine. The 2D representation of the ligand (e) The 2D representation with the color-coded rotatable bonds (f) The major ligand features observed during the MD simulation of 100 ns such as ligand RMSD, the radius of gyration (rGyr), intramolecular hydrogen bonds (intraHB), molecular surface area (MolSA), solvent accessible surface area (SASA) and polar surface area (PSA) monitored throughout the simulation (g) The torsion profiles (dial plot and bar plot) of the ligand for the rotatable bond is shown in various colors.

1536 **Supplementary Tables**

1537 **Table S1**. Computational virtual screening of selected natural lead molecules by literature

1538 survey and database search based on the drug likeliness features predicted by PreADMET

1539 and SwissADME

1540 **Table S2**. The prediction of ADME features of the natural lead molecules, which qualified

1541 the drug likeliness features via various statistical models available in PreADMET and

1542 SwissADME.

1543 **Table S3**. The prediction of toxicity features of the natural lead molecules that qualified the

1544 ADME features via various statistical models available in PreADMET and SwissADME.

Tables

Table 1. The structural description of eleven probable drug targets (with known 3D structures) that are involved in the virulence and pathogenesis of SARS-CoV-2

PDB ID	Name of the protein	Chain	Resolution	R-Value Free	R-Value Work	Experimental method	Secondary structure	References
1WYY	Post-fusion hairpin conformation of the spike glycoprotein	A, B	2.2 Å	0.249	0.210	X-ray diffraction	66% helical	Duquerroy et al., 2005
6VYB	SARS-CoV-2 spike ectodomain structure (open state)	A, B, C	3.2 Å	Aggregation state: Particle	Reconstruction method: Single particle	Electron Microscopy	16% helical, 25% beta sheet	Walls et al., 2020
6VXX	Structure of the SARS-CoV-2 spike glycoprotein (closed state)	A, B, C	2.8Å	Aggregation state: Particle	Reconstruction method: Single particle	Electron Microscopy	16% helical, 25% beta sheet	Walls et al., 2020
1Q2W	X-Ray Crystal Structure of the SARS Coronavirus Main Protease	A, B	1.86 Å	0.249	0.194	X-ray diffraction	24% helical, 28% beta sheet	Bonanno et al., 2003
5RE4	Crystal Structure of SARS-CoV-2 main protease in complex with Z1129283193	A	1.88Å	0.266	0.199	X-ray diffraction	26% helical, 28% beta sheet	Fearon et al., to be published
3I6G	Newly identified epitope Mn2 from SARS-CoV M protein complexed withHLA-A*0201	C, F	2.201Å	0.246	0.205	X-ray diffraction	26% helical, 39% beta sheet	Liu et al., 2010
2MM4	Structure of a Conserved Golgi Complex-targeting Signal in Coronavirus Envelope Proteins	A	-	Conformers Calculated: 200	Conformers Submitted: 15	NMR	65% helical	Li et al., 2014
1XAK	Structure of the sars-coronavirus orf7a accessory protein	A	1.8Å	0.275	0.223	X-ray diffraction	48% beta sheet	Nelson et al., 2005
2CME	The crystal structure of SARS coronavirus ORF-9b protein	A	2.8Å	0.289	0.266	X-ray diffraction	3% helical, 44% beta sheet	Meier et al., 2006
6M17	The 2019-nCoV RBD/ACE2-B0AT1 complex	E, F	2.9Å	Aggregation state: Particle	Reconstruction method: Single particle	Electron Microscopy	3% helical, 23% beta sheet	Yan et al., 2020
6M71	SARS-Cov-2 RNA-dependent RNA polymerase in complex with cofactors	A, B. C, D	2.9Å	Aggregation state: Particle	Reconstruction method: Single particle	Electron Microscopy	47% helical, 17% beta sheet	Gao et al., 2020

Table 2. The computational validation description of 3 probable drug targets of SARS-CoV-2 causing COVID-19 that are involved in the pathogenesis mechanism of coronavirus modeled by ab initio approach using the C-I tasser server

UniProt ID	Organism	Entry names	Protein names	Gene	Function	Length	ProSA (z-score)	ERRAT (overall quality factor)	WHATIF Ramachandran (Z-score)	Verify3D (residues having averaged 3D-1D score >= 0.2)	Anolea (e/kt)	ProCheck		
												Favoured region	Allowed region	Outlier region
P59632	Human SARS coronavirus (SARS-CoV)	AP3A_CVHSA	Protein 3a	3a	induces apoptosis	274	-3.33	39.62	-5.763	50.82%	359	69%	35.8%	5.2%
P0C6U8	Human SARS coronavirus (SARS-CoV)	R1A_CVHSA	Non-structural protein 10	Nsp10	essential for viral mRNA cap methylation	139	-4.88	30.71	-6.042	63.64%	871	68.8%	27.9%	3.2%
P59634	Human SARS coronavirus (SARS-CoV)	NS6_CVHSA	Non-structural protein 6	Nsp6	induction of autophagosomes	63	-5.67	86.84	0.783	64.65%	-528	89.3%	9.1%	1.6%

Table 3. The binding potential of selected natural lead molecules towards the probable drug targets of human SARS-CoV-2 predicted by molecular docking studies by AutoDock and AutoDock Vina

Protein name	PDB ID	Ligand names	Ligand structure	Binding affinity (Kcal/mol)	RMSD (Å)	Interacting residues	Hydrogen bonds
Spike glycoprotein	1WYY	Hyoscyamine Pubchem ID: 154417 Source: *Datura stramonium*		-8.14	0.0	Ser924, Thr925, Gly928, Asp932, Gln1161, ILe1164, Asn1168 (Chain A), Ser924, Thr925, Gly928, Gln1161, Ile1164 (Chain B)	Asn1168: 2
Spike glycoprotein-Closed state	6VXX			-5.7	0.0	Leu335, Pro337, Phe338, Gly339, Asp364, Val367	0
Spike glycoprotein-Open state	6VYB			-6.0	0.0	Trp104, Ile119, Val126, Ile128, Tyr170, Ser172, Ile203, Val227	Ser172: 1
Membrane protein	3I6G			-0.7	0.0	Gly0	0
Envelope small membrane protein	2MM4			-2.2	0.0	Lys63, Asn64	0
Replicase polyprotein 1ab	1Q2W			-6.1	0.0	Glu156, Met165, Asp187, Arg188,Gln189, Gln192	Gln192
Replicase polyprotein 1a	5RE4			-6.0	0.0	Trp218, Asn221, Leu271	Trp218: 1
Protein 7a	1XAK			-4.4	0.0	Tyr3, Tyr5, His47, Gln61	0
Protein 9b	2CME			-4.4	0.0	Arg68, Ala69, Phe70	0
Receptor binding domain of membrane protein	6M17			-5.4	0.0	Thr376, Val407, Ala411, Val433, Tyr508	0
Non-structural protein 7	6M71_C			-5.3	0.0	Thr46, Phe49, Val53	0
Non-structural protein 8	6M71_B, D			-5.9	0.0	Leu128, Val130, Thr141, Tyr149	0

3

Protein	PDB ID	Ligand		Energy		Interacting residues	H-bonds
Non-structural protein 12	6M71_A			-5.4	0.0	Pro412, Phe415,Phe440, Phe843,	0
Non-structural Protein 6	Hypothetical model			-5.2	0.0	Asp6, Phe7, Leu15, Leu40, Ile60	0
Non-structural Protein 10	Hypothetical model			-6.1	0.0	Ile55, Cys74, Tyr76, His83, Asp91, Leu112, Thr115, Val116	His83:1
Protein 3a	Hypothetical model			-5.3	0.0	Phe56, Ile63, Lys66,Tyr189, Glu191,	0
Spike glycoprotein	1WYY	Rotiorinol C Pubchem ID: 11703984 Source: *Chaetorium cupreum*		-9.82	0.0	Arg4, Lys5, Tyr126, Gln127, Arg131, Asp289 and Glu290	5, Lys5, Gln127, Asp 289, Glu290 (A chain) Glu127 (B chain)
Spike glycoprotein- Closed state	6VXX			-6.2	0.0	Arg34, Thr208, Pro209, Leu212, Pro217, Gln218, Phe220	Phe220: 1
Spike glycoprotein- Open state	6VYB			-6.3	0.0	Thr33, Phe59, Asp287	0
Membrane protein	3I6G			-0.6	0.0	Gly0	0
Envelope small membrane protein	2MM4			-2.2	0.0	Lys63, Asn64	0
Replicase polyprotein 1ab	1Q2W			-7.0	0.0	Phe3, Lys5, Arg131, Trp207, Phe291, Ile286, Asp289	Trp207: 1
Replicase polyprotein 1a	5RE4			-6.7	0.0	Lys137, Thr199, Tyr239, Leu286,Leu287, Glu288, Asp289	Tyr239, Asp289: 3
Protein 7a	1XAK			-5.4	0.0	Tyr3, His47, Arg57, Thr59	0
Protein 9b	2CME			-5.0	0.0	Ser56, Leu65, Glu66, Ala67, Arg68, Ala69, Phe70, Ser72	Ser56: 1

4

Protein	PDB ID	Compound		Energy		Interacting residues	H-bond
Receptor binding domain of membrane protein	6M17			-6.1	0.0	Cys336, Phe338, Gly339, Ala363, Asp364, Val367,Ser371, Ser373, Phe374,	Ser373: 1
Non-structural protein 7	6M71_C			-5.9	0.0	Lys2, Asp5, Thr9, Thr46, Phe49, Val53, Met52	0
Non-structural protein 8	6M71_B, D			-6.0	0.0	Pro133, Asp134, Tyr135, Trp182, Pro178	Tyr135: 1
Non-structural protein 12	6M71_A			-6.6	0.0	Arg181, Gln184, Asn213	0
Non-structural protein 6	Hypothetical model			-5.6	0.0	Gln8, Lys38, Lys42, Leu44	Lys42: 1
Non-structural Protein 10	Hypothetical model			-6.8	0.0	Ile55, His83, Lys96,Val116	His83:1
Protein 3a	Hypothetical model			-6.3	0.0	Phe28, Val29, Arg68, Ala72, Val90	0
Spike glycoprotein	1wyy	Scutifoliamide A Chemspider ID: 23311285 Source: *Piper scutifolium*		-6.4	0.0	Asn910, Ala940, Thr943,Leu944, Gln947, Asn951,Leu1178,Leu1181, Glu1183	0
Spike glycoprotein-Closed state	6VXX			-5.4	0.0	Leu118, Val120, Phe135, Leu141, Leu241	0
Spike glycoprotein-Open state	6VYB			-6.6	0.0	Phe823, Asn824,Val826, Pro863,Pro1057,His1058	Asn824: 1
Membrane protein	3I6G			-0.7	0.0	Gly0	0
Envelope small membrane protein	2MM4			-0.8	0.0	Ly63	0
Replicase polyprotein 1ab	1Q2W			-6.9	0.0	Arg4, Lys5 and Phe291 (A chain), Lys 5 (B chain)	1; Lys5 (B chain)
Replicase polyprotein 1a	5RE4			-6.8	0.0	Val212, Arg217, Leu220, Gln256, Ile259, Asp263	0

5

Protein	PDB ID	Ligand/Source			Residues	H-bonds
Protein 7a	1XAK		-5.6	0.0	Gln6, Cys8,Val9, Thr12, Leu16, Lys17	Val9, Lys17: 2
Protein 9b	2CME		-4.4	0.0	Ala58, Arg68, Ala69, Phe70, Ser72	0
Receptor binding domain of membrane protein	6M17		-5.9	0.0	Gln493, Tyr495, Gly502, Tyr505	Gln493, Gly502: 2
Non-structural protein 7	6M71_C		-5.9	0.0	Asp5, Thr9, Thr46, Phe49, Glu50, Val53	Thr9: 1
Non-structural protein 8	6M71_B, D		-6.0	0.0	Leu128, Met129, Pro133, Thr141, Tyr149	0
Non-structural protein 12	6M71_A		-6.1	0.0	Asp484, Ile488, Gln573, Ser578, Ala581	0
Non-structural Protein 6	Hypothetical model		-5.5	0.0	Leu16, Ile17, Arg20, Thr21	Arg20: 1
Non-structural Protein 10	Hypothetical model		-5.6	0.0	His83, Leu92, Asn114, Thr115,Val116	Val116: 2
Protein 3a	Hypothetical model		-5.4	0.0	Cys130, Trp131, His150, His204, His227	0
Spike glycoprotein	1wyy	Tamaridone Pubchem ID: 15345466 Source: *Tamarix dioica*	-7.2	0.0	Asp931, Asn935, Lys1162, Asp1165, Asn1168, Lys1172	1; Asn935
Spike glycoprotein-Closed state	6VXX		-7.3	0.0	Ala520, Phe559, Phe562, Gln563, Gln564, Phe565, Gly566, Arg567	Gln564, Phe565, Arg567: 4
Spike glycoprotein-Open state	6VYB		-6.8	0.0	Thr732, Thr778, Ser780, Pro863, His1058	Ser730: 2
Membrane protein	3I6G		-0.8	0.0	Gly0	0
Envelope small membrane protein	2MM4		-3.1	0.0	Lys63, Asn64	Asn64: 1
Replicase polyprotein 1ab	1Q2W		-6.3	0.0	Gly11, Lys12, Glu14, Gly15,	Gly11: 1

Replicase polyprotein 1a	5RE4		-7.0	0.0	Leu87, Lys137, Thr190, Tyr237, Tyr239, Leu285	Tyr237: 1
Protein 7a	1XAK		-5.7	0.0	Val9, Thr12, Val14, Arg65	0
Protein 9b	2CME		-5.6	0.0	Arg68, Gln71, Ser72	0
Receptor binding domain of membrane protein	6M17		-6.5	0.0	Thr345, Arg346, Ser349, Lys441, Lys444, Asn448, Asn450, Tyr451	Lys444: 1
Non-structural protein 7	6M71_C		-5.9	0.0	Lys2, Val6, Thr9, Phe49, Met52	Thr9: 1
Non-structural protein 8	6M71_B, D		-5.7	0.0	Leu128, Val130, Val131, Thr141, Tyr149	0
Non-structural protein 12	6M71_A		-6.7	0.0	Lys47, His133, Asn138, Lys780	0
Non-structural Protein 6	Hypothetical model		-5.6	0.0	Lys48, Ser50, Leu52, Asp53, Gln56	Leu52: 1
Non-structural Protein 10	Hypothetical model		-6.7	0.0	Pro37, Asn105, Asp106, Phe110, Lys113, Asn114, Tyr126	Asn105, Asn114: 2
Protein 3a	Hypothetical model		-6.6	0.0	Gln213, Val255, Ile263, Thr270	0

7

(a)

(b)

M D L F M R I F T I G T V T L K Q G E I K D A T P S D F V R A T A T I P I Q A S L P F G W L I V G V
A L L A V F Q S A S K I I T L K K R W Q L A L S K G V H D F V C N L L L L F V T V Y S H L L L V A A G
L E A P F L Y L Y A L V Y F L Q S I N F V R I I M R L W L C W K C R S K N P L L Y D A N Y F L C W H
T N C Y D Y C I P Y N S V T S S I V I T S G D G T T S P I S E H D Y Q I G Y T E K W E S G V K D Q V
V V L H S Y F T S D Y Y Q L Y S T Q L S T D T G V E H V T F F I Y N K I V D E P E E H V Q I H T I D
G S S G V V N P V M E P I Y D E P T T T S V P L

(c)

(d)

X-ray
NMR

Z score: -4.88

(e)

Averaged Score   Raw Score

(f)

99% Error

95% Warning

(a)

(b)

M F H L V D F Q V T I A E I L L I I M R T F K V S I W N L D Y I I N L I I K N L S K S L T E N K Y S

Q L D E E Q P M E I D

(c)

(d)

Z score: -3.33

(e)

(f)

ERRAT Error Values

99% Error

95% Warning

(a)

(b)

A G N A T E V P A N S T V L S F C A F A V D A A K A Y K D Y L A S G G Q P I T N C V K M L C T H T G

T G Q A I T V T P E A N M D Q E S F G G A S C C L Y C R C H I D H P N P K G F C D L K G K Y V Q I P

T T C A N D P V G F T L K N T V C T V C G M W K G Y G C S C D Q L R E P M L Q
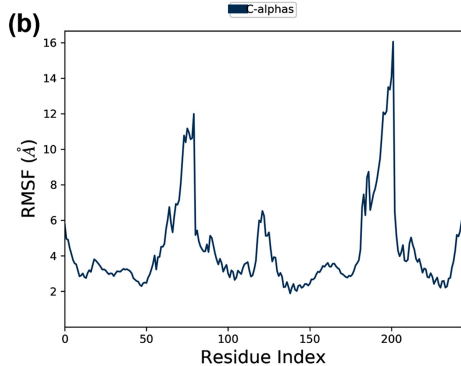
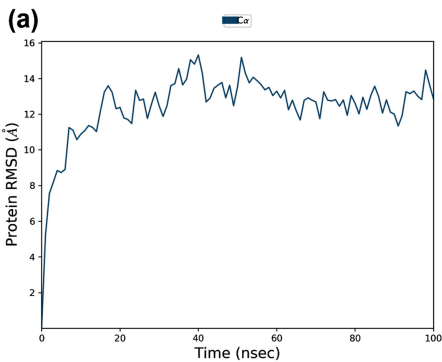(c)

(d)

Z score: -4.05

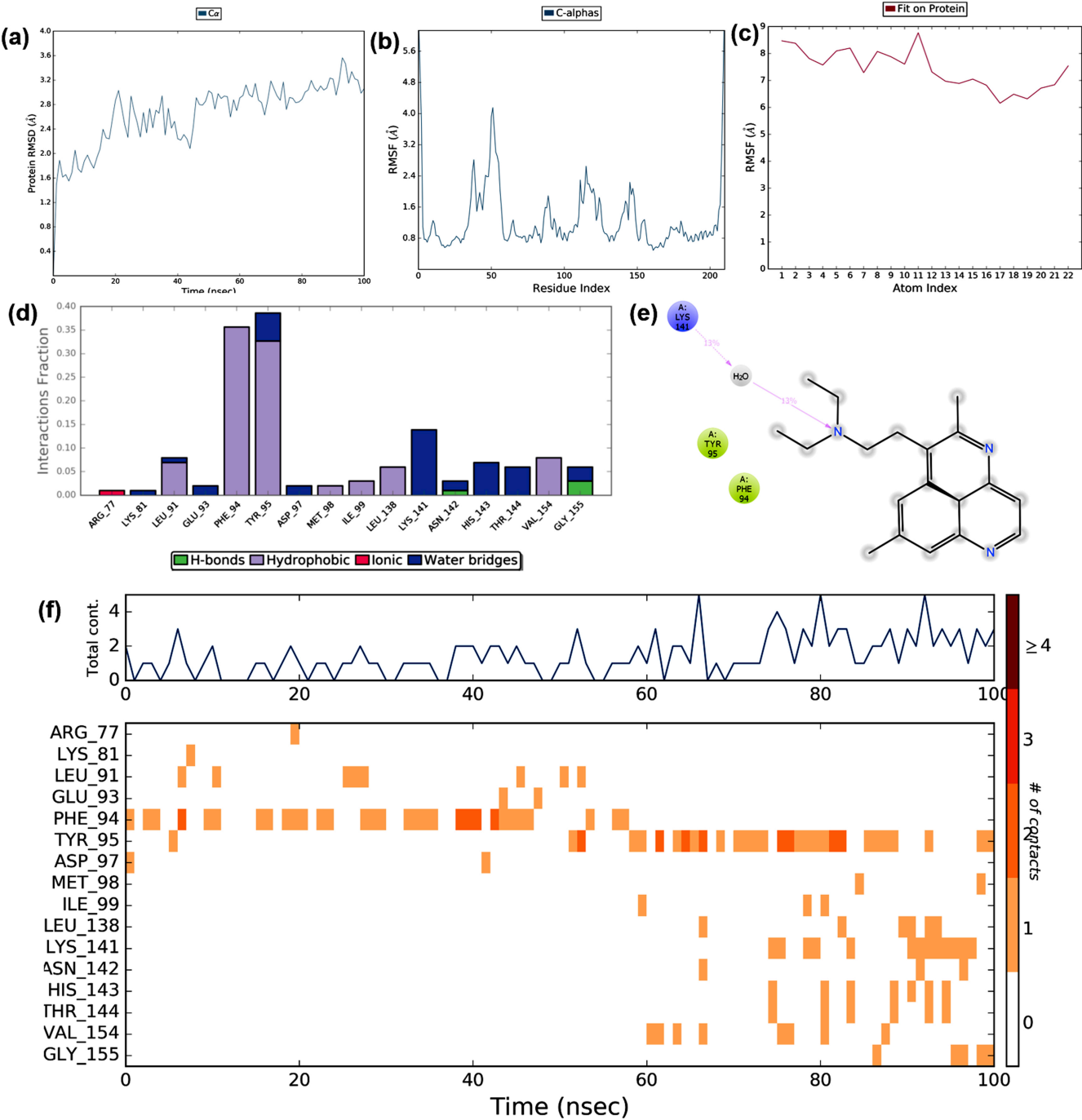(e)

(f)

(a) (b) (c) (d)

Highlights

- Aimed to study the binding potential of natural lead molecules to SARS-CoV-2 targets
- Four lead molecules showed the binding potential to the selected targets of S SARS-CoV-2
- Hyoscyamine and Tamaridone showed the profound binding potential to spike glycoprotein
- Rotiorinol-C and Scutifoliamide-A showed significant binding to the main protease of SARS-CoV-2
- Natural leads showed better binding than currently suggested antiviral drugs

Conflict of interest statement

The authors declare that they have no competing interests.